APR 1 0 1979

DEC 1 5 1982
JUL 0 3 1985

CALCULATION OF SKIN FRICTION IN
TWO-DIMENSIONAL, TRANSONIC, TURBULENT FLOW

T. W. Swafford

ARO, Inc., a Sverdrup Corporation Company

PROPULSION WIND TUNNEL FACILITY
ARNOLD ENGINEERING DEVELOPMENT CENTER
AIR FORCE SYSTEMS COMMAND
ARNOLD AIR FORCE STATION, TENNESSEE 37389

April 1979

TECHNICAL REPORTS
FILE COPY

Final Report for Period October 1977 — September 1978

Property of U. S. Air Force
A E D C L I B R A R Y
F 4 0 6 0 0 - 7 7 - C - 0 0 0 3

Prepared for

ARNOLD ENGINEERING DEVELOPMENT CENTER/DOTR
ARNOLD AIR FORCE STATION, TENNESSEE 37389

This report has been reviewed by the Information Office (OI) and is releasable to the National Technical Information Service (NTIS). At NTIS, it will be available to the general public, including foreign nations.

APPROVAL STATEMENT

This report has been reviewed and approved.

ELTON R. THOMPSON
Project Manager, Research Division
Directorate of Test Engineering

Approved for publication:

FOR THE COMMANDER

ROBERT W. CROSSLEY, Lt Colonel. USAF
Acting Director of Test Engineering
Deputy for Operations

REPORT DOCUMENTATION PAGE		READ INSTRUCTIONS BEFORE COMPLETING FORM
1 REPORT NUMBER AEDC-TR-79-12	2 GOVT ACCESSION NO.	3 RECIPIENT'S CATALOG NUMBER
4 TITLE (and Subtitle) CALCULATION OF SKIN FRICTION IN TWO-DIMENSIONAL, TRANSONIC, TURBULENT FLOW		5 TYPE OF REPORT & PERIOD COVERED Final Report-October 1977 - September 1978
		6. PERFORMING ORG. REPORT NUMBER
7. AUTHOR(s) T. W. Swafford, ARO, Inc., a Sverdrup Corporation Company		8. CONTRACT OR GRANT NUMBER(s)
9 PERFORMING ORGANIZATION NAME AND ADDRESS Arnold Engineering Development Center/DOTR Air Force Systems Command Arnold Air Force Station, Tennessee 37389		10 PROGRAM ELEMENT, PROJECT, TASK AREA & WORK UNIT NUMBERS Program Element 65807F
11 CONTROLLING OFFICE NAME AND ADDRESS Arnold Engineering Development Center/OIS Arnold Air Force Station, Tennessee 37389		12. REPORT DATE April 1979
		13. NUMBER OF PAGES 47
14 MONITORING AGENCY NAME & ADDRESS(If different from Controlling Office)		15 SECURITY CLASS. (of this report) UNCLASSIFIED
		15a DECLASSIFICATION/DOWNGRADING SCHEDULE N/A

16 DISTRIBUTION STATEMENT (of this Report)

Approved for public release; distribution unlimited.

17 DISTRIBUTION STATEMENT (of the abstract entered in Block 20, if different from Report)

18 SUPPLEMENTARY NOTES

Available in DDC

19 KEY WORDS (Continue on reverse side if necessary and identify by block number)

computations	turbulent flow
skin friction	computer programs
two-dimensional flow	boundary layer
transonic flow	physical properties

20. ABSTRACT (Continue on reverse side if necessary and identify by block number)

An investigation of five computer programs which calculate skin friction and boundary-layer integral properties in two-dimensional, turbulent, transonic flow was conducted. The five programs were of varying complexity and consisted of four boundary-layer-type methods with turbulence modeling varying from algebraic eddy viscosity models to a two-equation of turbulence model, and one mean flow compressible Navier-Stokes technique

DD FORM 1473 JAN 73 EDITION OF 1 NOV 65 IS OBSOLETE

20. ABSTRACT (Continued)

with algebraic turbulence modeling. The quality of the computed results was judged by comparison with available experimental data. For the data considered (which were nonseparated, two-dimensional, transonic, adiabatic wall data), the most accurate calculations of skin friction were provided by an integral boundary-layer method and a finite difference boundary-layer method, both with algebraic turbulence modeling. These two calculation techniques were also the simplest to use and required less computational resources than the other calculation methods considered. However, these results must be tempered by the fact that all computational procedures could not be started from identical initial conditions. Moreover, separated and nonseparated flows with wall blowing, suction, and heat transfer were not considered.

AFSC
Arnold AFB Tenn

PREFACE

CONTENTS

ILLUSTRATIONS

TABLES

1.0 INTRODUCTION

The contribution of skin friction drag to total drag is frequently required in transonic aerodynamic testing. This occurs, for example, when total drag measurements are made in tunnel tests where flight Reynolds numbers cannot be duplicated. In such cases, the friction drag corresponding to test Reynolds number must be extracted from the tunnel data and replaced by the friction drag corresponding to flight Reynolds number. Such data manipulations must be accomplished by the application of correlation or prediction techniques. Therefore, the objective of the work described herein was to determine a suitable theoretical procedure for the calculation of skin friction drag in transonic turbulent flows at arbitrary Reynolds numbers. Of primary interest is the accuracy of the calculation method; however, it would be advantageous if the computation technique were also fast and required a minimal amount of computational resources.

Boundary layers over two-dimensional planar and axisymmetric bodies in transonic, turbulent flow were computed using five theoretical calculation techniques and the results are compared with experimental data. In addition to skin friction, other boundary-layer parameters are compared to provide a more complete test of the computational techniques.

The calculation methods chosen for evaluation are presented in Table 1 in order of increasing complexity with respect to basic formulation and turbulence modeling. Also shown in Table 1 are the machine requirements (in terms of the AEDC IBM 370/165) and extended capabilities (second-order boundary-layer effects) pertaining to each calculation procedure. The capabilities of each method are described in more detail in Section 2.0.

Experimental results were chosen from two investigations: a planar, supercritical airfoil experimental study (Ref. 1), and an investigation involving an axisymmetric, waisted body of revolution (Ref. 2). Both experimental studies were concerned with the measurement of mean flow turbulent boundary-layer properties at transonic speeds and adiabatic wall conditions.

2.0 CALCULATION METHODS

The calculation techniques evaluated can be classed in three categories which are the integral boundary-layer equations, finite difference boundary-layer equations, and the ensemble averaged, compressible, Navier-Stokes equations. The computational techniques used are documented elsewhere and only brief descriptions of the equations solved and the numerics and inputs required are given.

Table 1. Requirements and Extended Capabilities of Computational Methods

now running at 0.01 dd?

Method Name	Method Type	Computer Requirements			Extended Capabilities						
		Memory Required, K-bytes, IBM 370/165	Typical CPU Time, min, IBM 370/165	Relative Preparation Time — Prep. Time for Method 1	Turbulence Model	Transverse Curvature	Longitudinal Curvature	Free-Stream Turbulence	Wall Roughness	Wall Transpiration	Transition
Whitfield	Integral Boundary Layer	40	0.25	1	Algebraic						
Herring-Mellor	Finite Difference Boundary Layer	130	0.5	1.5	Algebraic	X			X	X	x^1
ABLE II	Finite Difference Boundary Layer	165	6.0	1.5	1-Equation of Turbulence	X				X	x^2
Wilcox	Finite Difference Boundary Layer	265	7.0	3	2-Equation of Turbulence	X		X	X	X	x^3
Deiwert	Finite Difference Navier-Stokes	480	100	20	Algebraic	X	X			X	x^1

[1] Artificial—user can specify the relative proportions of laminar and turbulent viscosities with axial variation

[2] Location of transition can be controlled by specifying amount of TKE in the layer

[3] Same as 2 with addition of controlling transition by also specifying turbulence length scale

2.1 INTEGRAL BOUNDARY-LAYER METHOD, WHITFIELD PROGRAM

The integral boundary-layer technique used is described in Ref. 3. Not unlike other integral methods, this technique involves transforming the partial differential equations of the boundary layer into ordinary differential equations in terms of integral parameters, i.e., the displacement thickness, δ^*, momentum thickness, θ, etc. The approach is to simultaneously solve the momentum integral equation

$$\frac{1}{r_w^k \rho_e U_e^2} \frac{d}{dx} (r_w^k \rho_e U_e^2 \theta) + \frac{\delta^*}{U_e} \frac{dU_e}{dx} = \frac{C_{f,e}}{2} \tag{1}$$

and the mean-flow kinetic energy integral equation

$$\frac{1}{2r_w^k \rho_e U_e^3} \frac{d}{dx} (r_w^k \rho_e U_e^3 \theta^*) + \frac{\delta^{**}}{U_e} \frac{dU_e}{dx} = \frac{C_{f,e}}{2} D \tag{2}$$

where

$$\delta^{**} = \int_0^\infty \frac{u}{U_e} \left(1 - \frac{\rho}{\rho_e}\right) dy \tag{3}$$

$$\theta^* = \int_0^\infty \frac{\rho u}{\rho_e U_e} \left(1 - \frac{u^2}{U_e^2}\right) dy \tag{4}$$

$$D = \int_0^\infty \frac{\tau_0}{\tau_w} \frac{\partial}{\partial y} \left(\frac{u}{U_e}\right) dy \tag{5}$$

Equations (1) and (2) are valid for two-dimensional planar (k = 0) flow, and axisymmetric (k = 1) flow with the terms involving the transverse curvature effects neglected. The main advantage of this method over other integral techniques is attributed to two recent developments: (1) the improved anlaytical description of the compressible, turbulent boundary-layer velocity profile presented in Ref. 4, where it is shown that the entire turbulent boundary layer can be reasonably well described by one analytical expression involving the shape factor, H, skin friction coefficient, $C_{f,e}$, and Reynolds number based on boundary-layer momentum thickness, Re_θ, and (2) the improved velocity-temperature expression for turbulent boundary layers with nonunity Prandtl numbers, developed in Ref. 5.

To describe the effect of turbulence within the boundary layer (i.e., to model the Reynolds stress term), a three-layer, algebraic, eddy viscosity model is used. In the region nearest the wall ($y^+ < 100$), the total shear stress (molecular plus turbulent) is assumed constant and equal to the wall value. The eddy viscosity in the middle region ($y^+ > 100$, $\epsilon_m < \epsilon_o$) is given by (Ref. 6)

7

$$\epsilon_m = (0.41y)^2 \left| \frac{\partial u}{\partial y} \right| \tag{6}$$

In the outer region (defined for y greater than the minimum y where $\epsilon_o = \epsilon_m$), a constant eddy viscosity as suggested by Clauser (Ref. 7) is used:

$$\epsilon_o = 0.0168 \, U_e \bar{\delta}^* \tag{7}$$

where

$$\bar{\delta}^* = \int_o^\infty \left(1 - \frac{u}{U_e} \right) dy \tag{8}$$

The integral equations of the boundary layer are then cast into finite difference form and solved by the predictor-corrector method used by Nash (Ref. 8). Inputs required for the program include initial values of shape factor, momentum thickness, free-stream Mach and Reynolds numbers, and the axial variation of edge Mach number and body surface radius (for axisymmetric flow). For the comparisons presented herein, the measured values of shape factor and momentum thickness at the first measurement station were used as initial conditions from which the initial value of $C_{f,e}$ is determined from a correlation of $C_{f,e} = C_{f,e}(Re_\theta, H)$ (Ref. 3).

2.2 FINITE DIFFERENCE BOUNDARY-LAYER METHODS

2.2.1 Herring-Mellor Program

The method of Herring and Mellor (Refs. 9 and 10) encompasses the solution of the compressible, two-dimensional (planar or axisymmetric), laminar and/or turbulent boundary-layer equations. The equations solved are

$$\frac{\partial}{\partial x}(r\rho u) + \frac{\partial}{\partial y}(r\rho v) = 0 \tag{9}$$

$$\rho u \frac{\partial u}{\partial x} + \rho v \frac{\partial u}{\partial y} = \rho_e U_e \frac{dU_e}{dx} + \frac{1}{r} \frac{\partial}{\partial y}(r\tau_o) \tag{10}$$

$$\rho u \frac{\partial h_o}{\partial x} + \rho v \frac{\partial h_o}{\partial y} = \frac{1}{r} \frac{\partial}{\partial y}\left[r(q_o + u\tau_o) \right] \tag{11}$$

which are valid for either laminar or turbulent flow if τ_o and q_o are defined as the total shear stress and total heat flux, respectively,

$$\tau_o / \rho = \nu \frac{\partial u}{\partial y} - \langle u'v' \rangle \tag{12}$$

$$q_o/\rho = k\frac{\partial h}{\partial y} - \langle v'h'\rangle \tag{13}$$

The gross effects of turbulence are simulated by using the "effective viscosity hypothesis" of Mellor (Ref. 11). The effective viscosity for the total boundary layer is given by

$$\nu_{ef} = U_e\bar{\delta}^* \left[\frac{\phi(X\,\tilde{R})}{\tilde{R}} + \Phi(X) - X\right] \tag{14}$$

and the effective conductivity by

$$a_{ef} = U_e\delta^* \left[\frac{\frac{\nu}{\nu_\infty}}{Re_{\bar{\delta}}^* P_r} + \frac{1}{P_{r_t}}\left(\frac{\nu_{ef}}{U_e\bar{\delta}^*} - \frac{\frac{\nu}{\nu_\infty}}{Re_{\bar{\delta}}^*}\right)\right] \tag{15}$$

where

$$X = \frac{0.41y\sqrt{\frac{\tau_o}{\rho}}}{\bar{\delta}^*U_e} \tag{16}$$

$$\tilde{R} = \frac{\bar{\delta}^*U_e}{\nu} \tag{17}$$

$$\phi = 1 + \frac{\chi^4}{\chi^3 + (6.9)^3}, \quad \chi = \tilde{R}X \tag{18}$$

$$\Phi = X\ (X<0.016),\ \Phi = 0.016\ (X>0.016) \tag{19}$$

Considerable flexibility is possible in terms of the specification of boundary conditions. Provisions have been made to include the effects of wall transpiration and roughness as well as the capacity of treating an adiabatic wall and/or variable wall temperature case. An artificial method of simulating transition can be effected by specifying the amount and location of turbulent viscosity to be linearly combined with the molecular viscosity (Ref. 10).

To effect a solution. the boundary-layer equations (Eqs. 9 through 11) are first transformed into an intermediate form by using a modified version of the Probstein-Elliot transformation (Ref. 12). Then, by utilizing axial direction finite differences, the equations are transformed again into ordinary differential equations. The equations are then written for each grid point across the boundary layer and the resulting characteristic matrix is solved by Gaussian elimination. Initial velocity and temperature profiles (either laminar or turbulent), boundary-layer-edge velocity distribution, and any wall conditions pertaining to the specification of wall temperature distribution (or an adiabatic wall), wall

roughness, or transpiration are required for initialization of the program. (It is worthy to note that the incompressible version of the program received a "good" rating from the 1968 "Boundary Layer Olympics" held at Stanford University (Ref. 13.)). In this case, the initial turbulent velocity profile was generated by using the results of Ref. 4 and the first measured values of $C_{f,e}$, H, and θ.

2.2.2 ABLE-II Program*

Similar to the equations solved by the Herring-Mellor method, the ABLE-II program ("ABLE" referring to "Algorithm for Boundary Layer Type Equations" of Patankar and Spalding (Ref. 14)) obtains a finite-difference solution to the compressible, two-dimensional (planar or axisymmetric), laminar and/or turbulent boundary-layer equations, taking into account any effects of wall transpiration and transverse curvature (longitudinal curvature and wall roughness effects are neglected). Calculations can also be made with an adiabatic wall and/or variable wall temperature. In terms of nondimensional variables, the equations solved by the ABLE-II method are

$$\frac{\partial}{\partial \bar{x}} (\bar{\rho}\,\bar{r}\,\bar{u}) + \frac{\partial}{\partial \bar{y}} (\bar{\rho}\,\bar{r}\,\bar{v}) = 0 \tag{20}$$

$$\bar{\rho}\bar{u}\frac{\partial \bar{u}}{\partial \bar{x}} + \bar{\rho}\,\bar{v}\frac{\partial \bar{u}}{\partial \bar{y}} = -\frac{\partial \bar{p}}{\partial \bar{x}} + \frac{1}{\bar{r}}\frac{\partial}{\partial \bar{y}}\left\{\bar{r}\left[\frac{\sqrt{2}\,\bar{\mu}}{Re_{o,s}} - \frac{\bar{\rho}<u'v'>}{\frac{\partial \bar{u}}{\partial \bar{y}}}\right]\frac{\partial \bar{u}}{\partial \bar{y}}\right\} \tag{21}$$

$$\bar{\rho}\bar{u}\frac{\partial \bar{h}_o}{\partial \bar{x}} - \bar{\rho}\bar{v}\frac{\partial \bar{h}_o}{\partial \bar{y}} = \frac{1}{\bar{r}}\frac{\partial}{\partial \bar{y}}\left\{\bar{r}\left[\left(\frac{\sqrt{2}\,\bar{\mu}}{Re_{o,s}} - \frac{\bar{\rho}<u'v'>}{Pr_t\frac{\partial \bar{u}}{\partial \bar{y}}}\right)\frac{\partial \bar{h}_o}{\partial \bar{y}}\right.\right.$$

$$\left.\left. -\frac{\sqrt{2}\,\bar{\mu}}{Re_{o,s}}\left(1-\frac{1}{Pr}\right)\bar{u}\frac{\partial \bar{u}}{\partial y} - \frac{\bar{\rho}<u'v'>}{\frac{\partial \bar{u}}{\partial \bar{y}}}\left(1-\frac{1}{Pr_t}\right)\bar{u}\frac{\partial \bar{u}}{\partial \bar{y}}\right]\right\} \tag{22}$$

where

$$Re_{o,s} = \frac{\rho_o(2h_{o,\infty})^{\frac{1}{2}}\,S}{\mu_o} \tag{23}$$

$$\bar{r} = \bar{r}_w \pm \bar{y}\cos\bar{\beta} \tag{24}$$

---

*This program was developed by Dr. J. A. Benek, ARO, Inc., and is not reported elsewhere.

The plus sign in Eq. (24) is for external flow, the minus sign for internal flow.

Computation of the Reynolds stress goes beyond the simple algebraic eddy viscosity concept in that the following particular partial differential equation (Ref. 15) describing the turbulent kinetic energy (TKE) across the boundary layer

$$\bar{\rho}\,\bar{u}\,\frac{\partial \bar{e}}{\partial \bar{x}} + \bar{\rho}\,\bar{v}\,\frac{\partial \bar{e}}{\partial \bar{y}} = \frac{1}{\sigma_e}\,\frac{1}{\bar{r}}\,\frac{\partial}{\partial \bar{y}}\left\{\bar{r}\left[\frac{\sqrt{2}\,\bar{\mu}}{Re_{o,s}} - \frac{\bar{\rho}<\overline{u'v'}>}{\frac{\partial \bar{u}}{\partial \bar{y}}}\right]\frac{\partial \bar{e}}{\partial \bar{y}}\right\}$$

$$- \bar{\rho}<\overline{u'v'}>\frac{\partial \bar{u}}{\partial \bar{y}} - \frac{c\,\bar{e}}{\bar{l}^2}\left[\frac{\sqrt{2}\,\bar{\mu}}{Re_{o,s}} - \frac{\bar{\rho}<\overline{u'v'}>}{\frac{\partial \bar{u}}{\partial \bar{y}}}\right] \qquad (25)$$

where

$$-<\bar{u}'\bar{v}'> = 0.3\bar{e} \qquad (26)$$

is solved in conjunction with the boundary-layer equations, Eqs. (20 through 22). Laminar flow can be represented by setting the TKE across the boundary layer equal to zero. Transition to turbulent flow can be simulated by initially setting the TKE to some specified low value and allowing the turbulence to grow. It should be pointed out that although reasonably good mean-flow quantities can be computed through transition, the location of transition is not known a priori. The transition location can be adjusted by changing the input value of the maximum TKE in the layer.

The numerics of the program involve solving the boundary-layer equations in normalized von Mises coordinates by means of the Patankar-Spalding finite difference procedure (Ref. 14). Inputs required to obtain a solution are free-stream Mach and Reynolds numbers, axial pressure and wall temperature distributions, wall transpiration rates, and the initial starting velocity and temperature profiles, the latter being either laminar or turbulent. For the comparisons presented herein, the ABLE-II solutions were begun from near the stagnation point and the transition location was varied such that the calculated and measured values of momentum thickness at the first measuring station were approximately equal.

2.2.3 Wilcox Program

The Wilcox program (Ref. 16) solves the compressible, two-dimensional (planar or axisymmetric) boundary-layer equations for laminar and/or turbulent flow. The equations can be written as

$$\frac{\partial}{\partial x}(\rho u) + \frac{1}{r^k}\,\frac{\partial}{\partial y}(r^k \rho v) = 0 \qquad (27)$$

$$\rho u \frac{\partial u}{\partial x} + \rho v \frac{\partial v}{\partial y} = -\frac{\partial p}{\partial x} - \frac{1}{r^k} \frac{\partial}{\partial y} \left[r^k (\mu + \rho\epsilon) \frac{\partial u}{\partial y} \right] \tag{28}$$

$$\rho u \frac{\partial}{\partial x} (c_p T) + \rho v \frac{\partial}{\partial y} (c_p T) = u \frac{\partial p}{\partial x} + (\mu + \rho\epsilon) \left(\frac{\partial u}{\partial y} \right)^2$$

$$+ \frac{1}{r^k} \frac{\partial}{\partial y} \left\{ r^k \left[\frac{\mu}{Pr} \frac{\partial}{\partial y} (c_p T) - \rho q \right] \right\} \tag{29}$$

where q is given either by

$$q = \frac{\epsilon}{Pr_t} \frac{\partial}{\partial y} (c_p T)$$

or by simultaneously solving Eqs. (27 through 29) with the equation

$$\rho u \frac{\partial q}{\partial x} + \rho v \frac{\partial q}{\partial y} = -\frac{4}{9} \rho e \frac{\partial}{\partial y} (c_p T) - \frac{32}{81} \rho \omega q + \frac{1}{r^k} \frac{\partial}{\partial y} \left[r^k (\frac{\mu}{Pr} + 2\rho\epsilon) \frac{\partial q}{\partial y} \right] \tag{30}$$

The eddy diffusivity, ϵ, in Eqs. (29 through 30), is assumed to be related to the TKE by

$$\epsilon = \frac{e}{\omega} \tag{31}$$

where ω is the turbulent dissipation rate.

The turbulence model utilized is more sophisticated than those described previously in that two equations are solved for the turbulent viscosity, the TKE equation plus an equation describing the turbulent dissipation rate (TDR). The equations used by Ref. 16 for describing the TKE and TDR are

$$\rho u \frac{\partial e}{\partial x} + \rho v \frac{\partial e}{\partial y} + \frac{9}{2} \frac{u}{R_s} \rho\epsilon \frac{\partial u}{\partial y} = \left[\alpha^* \left| \frac{\partial u}{\partial y} - \frac{u}{R_s} \right| - \beta^* \omega \right] \rho e$$

$$+ \frac{1}{r^k} \frac{\partial}{\partial y} \left[r^k (\mu + \sigma^* \rho\epsilon) \frac{\partial e}{\partial y} \right] \tag{32}$$

$$\rho u \frac{\partial \omega^2}{\partial x} - \rho v \frac{\partial \omega^2}{\partial y} = \left\{ \alpha \left| \frac{\partial u}{\partial y} - \frac{u}{R_s} \right| - \left[\beta + 2\sigma \left(\frac{\partial \psi}{\partial y} \right)^{1/2} \right] \omega \right\} \rho \omega^2$$

$$+ \frac{1}{r^k} \frac{\partial}{\partial y} \left[r^k (\mu + \sigma\rho\epsilon) \frac{\partial \omega^2}{\partial y} \right] \tag{33}$$

where β, β^*, σ, and σ^* are constants, $\psi = e^{1/2}\omega$, and a and a^* are functions of molecular viscosity, TKE, and TDR.

Flows with boundary conditions such as wall roughness, transpiration, varying wall temperature and/or an adiabatic wall can be computed with relative ease.

In order to solve Eqs. (27 through 33), the physical boundary-layer coordinates are transformed to the computational plane by the Probstein-Elliot (Ref. 12) and Levy-Lees (Ref. 17) transformations. The resulting block tridiagonal system of algebraic equations is then solved by the method of Blottner, et al. (Ref. 18).

Inputs required for the program are the usual external conditions such as free-stream Reynolds number, variations of the boundary-layer-edge Mach number, axial wall temperature distribution (or an adiabatic wall), etc., plus a constant value of the free-stream turbulent kinetic energy and/or turbulence length scale. From the latter stipulation, it is necessary to begin all calculations from an initial laminar starting profile. Similar to the ABLE-II program, transition to turbulent flow can be controlled by varying the input values of free-stream TKE and/or the free-stream turbulence length scale. For the comparisons presented herein, the Wilcox solutions were begun from near the stagnation point and the transition location was varied such that the calculated and measured values of momentum thickness at the first measuring station were approximately equal.

2.3 FINITE DIFFERENCE NAVIER-STOKES--DEIWERT PROGRAM

The Deiwert program (Refs. 19 through 21) solves the time-dependent, ensemble-averaged (Refs. 22 and 23) compressible, two-dimensional, Navier-Stokes equations for arbitrary, two-dimensional planar geometries. It should be noted that since the equations have been ensemble-averaged, time-dependence corresponds here to a period much longer than that associated with turbulent fluctuations, e.g., see Ref. 22. The program is basically an extended and improved version of the MacCormack method (Ref. 24) originally introduced in 1969 (Ref. 25). The present program, however, casts the Navier-Stokes equations into integral form, whereas MacCormack's formulation is in differential form (Ref. 26). Written in vector-integral form, Deiwert formulates the time-dependent, compressible, mean-flow, Navier-Stokes equations as

$$\frac{\partial}{\partial t} \int_{vol} U d\,(vol) + \int_{S} \vec{H} \cdot \vec{n}\,ds = 0 \tag{34}$$

where

$$U = \begin{bmatrix} \rho \\ \rho u \\ \rho v \\ e_t \end{bmatrix} \quad , \quad \vec{H} = \begin{bmatrix} \rho \vec{V} \\ \rho u \vec{V} + \vec{\vec{\tau}} \cdot \vec{e}_x \\ \rho v \vec{V} + \vec{\vec{\tau}} \cdot \vec{e}_y \\ e_t \vec{V} + \vec{\vec{\tau}} \cdot \vec{V} - k \Delta T \end{bmatrix} \tag{35}$$

$$\vec{V} = u \vec{e}_x + v \vec{e}_y \tag{36}$$

$$\vec{\vec{\tau}} = \sigma_x \vec{e}_x \vec{e}_x + \tau_{xy} \vec{e}_x \vec{e}_y + \tau_{yx} \vec{e}_y \vec{e}_x + \sigma_y \vec{e}_y \vec{e}_y \tag{37}$$

$$\sigma_x = \frac{2}{3} \mu \left(\frac{\partial u}{\partial x} + \frac{\partial v}{\partial y} \right) - 2\mu \frac{\partial u}{\partial x} + p \tag{38}$$

$$\sigma_y = \frac{2}{3} \mu \left(\frac{\partial u}{\partial x} + \frac{\partial v}{\partial y} \right) - 2\mu \frac{\partial v}{\partial y} + p \tag{39}$$

$$\tau_{xy} = \tau_{yx} = -\mu \left(\frac{\partial u}{\partial y} + \frac{\partial v}{\partial x} \right) \tag{40}$$

and $\vec{e}_x$, $\vec{e}_y$ are unit vectors in the x and y directions, respectively, and $\vec{n}$ is a unit vector normal to a grid cell face.

A simple, two-layer, eddy viscosity turbulence model (Ref. 22) is employed within the boundary-layer region to simulate the effects of turbulent fluctuations on the mean flow. For boundary-layer flow, the turbulent viscosity is assumed to be

$$\epsilon = \rho \ell^2 \left| \frac{\partial u}{\partial y} + \frac{\partial v}{\partial x} \right| \tag{41}$$

where

$$\ell = 0.4y \left[1 - \exp \left(-y \frac{\sqrt{\rho \left(\frac{\partial u}{\partial y} \right)_w / \mu}}{26} \right) \right] \tag{42}$$

for the inner region and

$$\ell = 0.09\delta \tag{43}$$

for the outer region.

In principle, any physically plausible boundary conditions such as adiabatic or variable temperature walls and wall transpiration can be implemented (except for subscale wall conditions such as roughness). To simulate transition from laminar to turbulent flow, the total viscosity (molecular plus turbulent) is set equal to the molecular viscosity upstream of a specified axial location on the body. Downstream of this location, the eddy viscosity (computed from the algebraic model) is added to the molecular viscosity in the normal fashion.

The numerical method casts the equations into an integral, primitive variable, conservative form (e.g., see Ref. 27) and utilizes the predictor-corrector, finite difference method of MacCormack (Refs. 20 and 24) for solution. The method is impulsively started from uniform free-stream conditions imposed throughout the computational domain. The solution then evolves with time until a steady state is reached.

Because a rather extensive nonorthogonal grid (Ref. 20) must be generated before the program can be implemented, a considerable amount of effort is required to ensure that important features of the flow will be properly resolved. Thus, in general, the inputs to the program are significantly more cumbersome than those needed for previously described boundary-layer methods. For example. in order to generate a mesh around an airfoil. one must specify where and how the grid cells are distributed around the leading edge and along the chord. In addition, to gain computational efficiency in the normal direction to the surface (Ref. 28) the mesh is split into two or more regions. In regions where large flow gradients are anticipated, the grids describing these regions are exponentially stretched in order that acceptable numerical resolution can be achieved. In any case, creation of the proper grid is not a trivial matter. Therefore, care must be exercised in allocating the number and location of mesh points, the amount of stretching, etc., such that all pertinent features of the flow are reasonably well resolved numerically.

3.0 EXPERIMENTAL DATA

A literature search revealed that very little reliable, experimental, transonic, two-dimensional, turbulent boundary-layer data have been published. Only two appropriate experimental investigations were found. Both experimental studies were conducted in the Royal Aircraft Establishment's (RAE) transonic facilities.

3.1 RAE AIRFOIL (PLANAR)

The experimental study of Cook, McDonald. and Firmin (Ref. 1) was conducted in the RAE 8-ft by 6-ft (2.44 m by 1.83 m) slotted wall, transonic, continuous flow wind tunnel and involved the probing of the turbulent boundary layer over a planar, supercritical airfoil (chord = 0.61 m. maximum thickness = 73.76 mm). shown in Fig. 1,

at high subsonic free-stream Mach numbers and at various angles of attack and Reynolds numbers. The flow conditions ranged from subcritical ($M_{local} < 1$) at negative angle of attack to supercritical ($M_{local} > 1$) at positive angle of attack. Data acquired were surface pressure distributions and mean-flow boundary-layer profiles deduced from traverses of pitot and static pressure probes. Oil flow was also utilized to detect the location of boundary-layer separation. In the cases to be used herein, boundary-layer transition was artificially induced on the upper surface at three and eleven percent chord by surface roughness. It was determined that at some high Mach and Reynolds numbers the roughness height (762 μ at the high Mach number cases, 127 μ for the lower Mach numbers) was larger than would normally be used. The tests were conducted such that temperature equilibrium was achieved between the model and flow (adiabatic wall). For the cases to be presented, the tunnel pressure fluctuations were reported to be less than 1.2 percent of the free-stream dynamic pressure. Skin friction was inferred from the velocity profile measurements by utilizing the equivalent, incompressible logarithmic form of the velocity profile given by Winter and Gaudet (Ref. 29). Boundary-layer integral properties were defined such that any effects of pressure gradient normal to the surface could be accounted for (e.g., see Ref. 30).
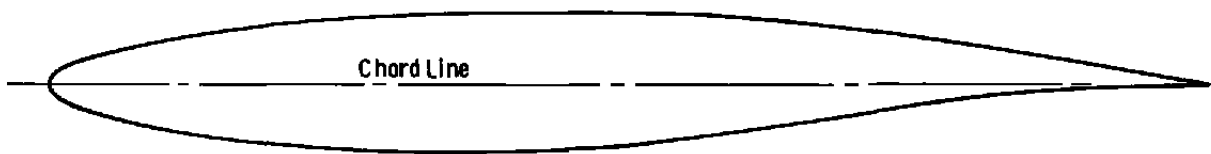

Figure 1. RAE 2822 airfoil cross section.

Surface pressures were the only measured quantities for which uncertainties were determined. At the low Reynolds number (2.7 x 10^6), the uncertainty in C_p was reported to be less than ±0.0064; at the high Reynolds number (6.5 x 10^6), less than ±0.0026. The airfoil angle of attack and tunnel Mach number settings were within ±0.01 deg and 0.001, respectively. Wall interference corrections were not included in the presentation of the data.

3.2 WAISTED BODY OF REVOLUTION

The wind tunnel investigation conducted by Winter, Rotta, and Smith (Ref. 2) using an axisymmetric, waisted body of revolution involved the detailed probing of the turbulent boundary layer as it developed over the body at high subsonic to low supersonic free-stream Mach numbers. The main objective of their study was to produce an axisymmetric, converging flow with an adverse pressure gradient in order to investigate the effects of Mach number, pressure gradient, and streamline convergence and divergence

on the development of the turbulent boundary layer. The model, shown in Fig. 2, was 1.524 m in length and had a maximum diameter of 0.254 m. The boundary layer was tripped near the nose of the body at approximately x/L = 0.025. The tests were conducted such that adiabatic wall conditions were achieved. Surface pressure measurements, mean-flow boundary-layer velocity profiles deduced from pitot pressure traverses, and surface skin friction determined by the razor blade technique (Ref. 31) were obtained. Measurements of tunnel free-stream turbulence were not reported. Boundary-layer integral properties, defined by

$$\tilde{\delta}^* = \int_0^\delta \left(1 - \frac{y}{r_w}\right)\left(1 - \frac{\rho u}{\rho_e U_e}\right) dy \tag{44}$$

$$\bar{\theta} = \int_0^\delta \left(1 + \frac{y}{r_w}\right) \frac{\rho u}{\rho_e U_e}\left(1 - \frac{u}{U_e}\right) dy \tag{45}$$

were evaluated by assuming the static pressure was constant through the boundary layer. The body radius term $(1 + y/r_w)$ was retained in the definitions so that the momentum integral equation could be used as a check on the validity of the experimentally determined boundary-layer integral parameters.
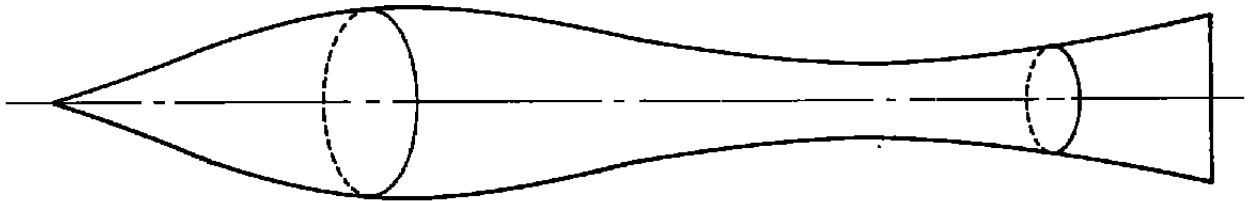

Figure 2. Waisted body of revolution.

It was noted in Ref. 2 that the validity of surface skin frictions obtained by the razor blade technique is questionable since it has not been fully validated in transonic flows with pressure gradients (also, see the comments of Rubesin, et al., in the introduction of Ref. 32).

Surface pressure coefficients were reported to be within ±0.005 for a Reynolds number of 10^7 while skin friction coefficients were estimated to be accurate to within ±0.0002, assuming that the calibration procedure (Ref. 31) is valid. The model shape was correct to within 0.01 in. (0.254 mm) of the design shape while the slope was constructed to within 0.001 in./in. (0.0254 mm/mm) of design.

4.0 RESULTS AND DISCUSSION

4.1 RAE AIRFOIL

The experiments of Ref. 1 with the RAE 2822 supercritical airfoil (Fig. 1) represent commonly encountered two-dimensional, transonic, airfoil-type flow fields (both subcritical and supercritical). Boundary-layer measurements were only made on the upper surface. Three sets of measurements were considered, denoted as Cases 2, 9, and 12. Case 2 ($M_\infty = 0.676$, $Re_{\infty,c} = 5.7 \times 10^6$, $a = -2.18$ deg) represents a fully subcritical flow with generally mild favorable and adverse pressure gradients on the upper surface. Case 9 ($M_\infty = 0.73$, $Re_{\infty,c} = 6.5 \times 10^6$, $a = 3.19$ deg) and Case 12 ($M_\infty = 0.73$, $Re_{\infty,c} = 2.7 \times 10^6$, $a = 3.19$ deg) are representative supercritical airfoil flows with severe adverse pressure gradients caused by shocks on the airfoil's upper surface.

4.1.1 Pressure Distributions

The measured airfoil surface pressure distributions are shown in Figs. 3a, b, and c for Cases 2, 9, and 12. respectively. Also shown are the surface pressures computed by the Deiwert program (recall that the external flow field is calculated by the Navier-Stokes method, whereas the boundary-layer methods require information about the external flow field as input).

Figure 3a illustrates that agreement between computed and measured surface pressures for Case 2 is not good, particularly on the upper surface where the computed results tend to exhibit oscillations upstream of about 50-percent chord possibly caused by relatively large axial grid spacing. Lower surface calculations are somewhat smoother but fall short of accurately computing the extent of expansion on the initial portion of the airfoil. In contrast, Fig. 3b shows good agreement between computed and measured airfoil surface pressure distributions. The calculated shock location and strength agree remarkably well with the measured data. Lower surface calculations again fall below the quantitative expansion of the measured data. The measured and computed airfoil surface pressures at lower Reynolds number, shown in Fig. 3c, illustrate fair agreement between experiment and calculation. On the upper surface, the shock location was computed to be downstream of the experimental location. Also, the expansion peak indicated by the experimental data at approximately seven-percent chord is underpredicted by the calculations as are the lower surface computations over the entire chord length. Good agreement is achieved. however, between the calculations and experiments on the upper surface downstream of 65-percent chord.
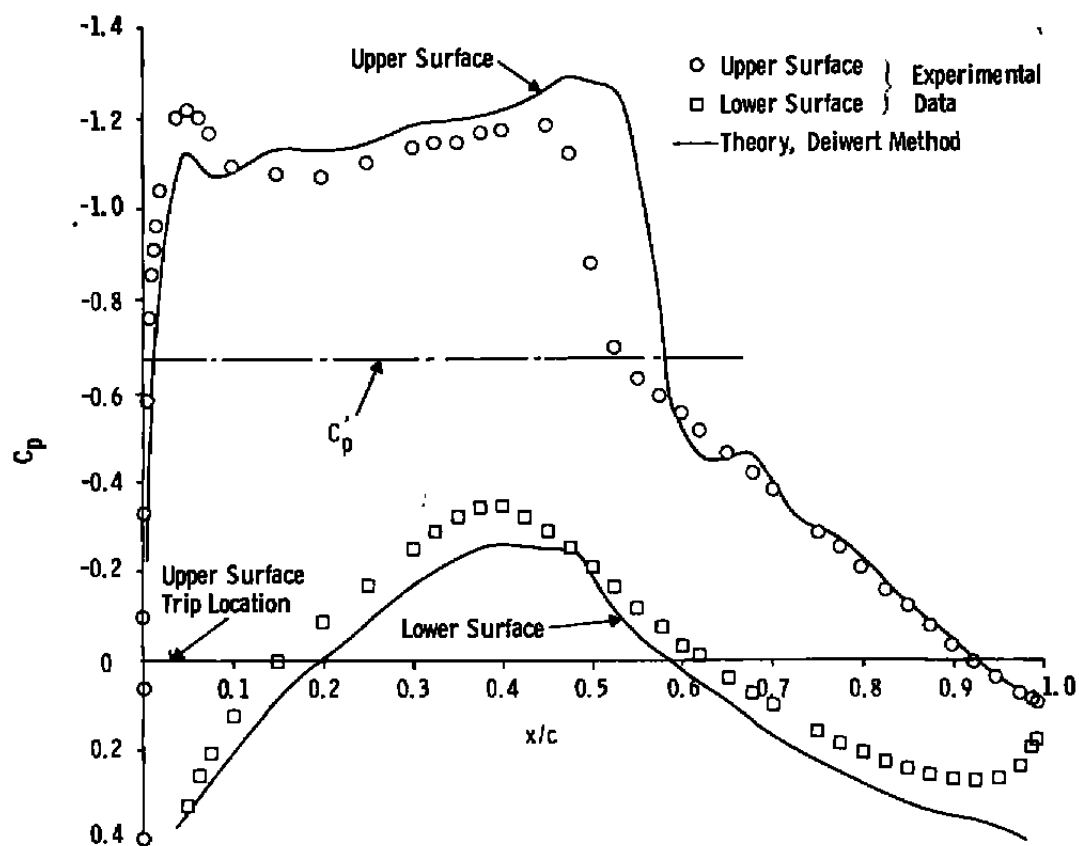
18
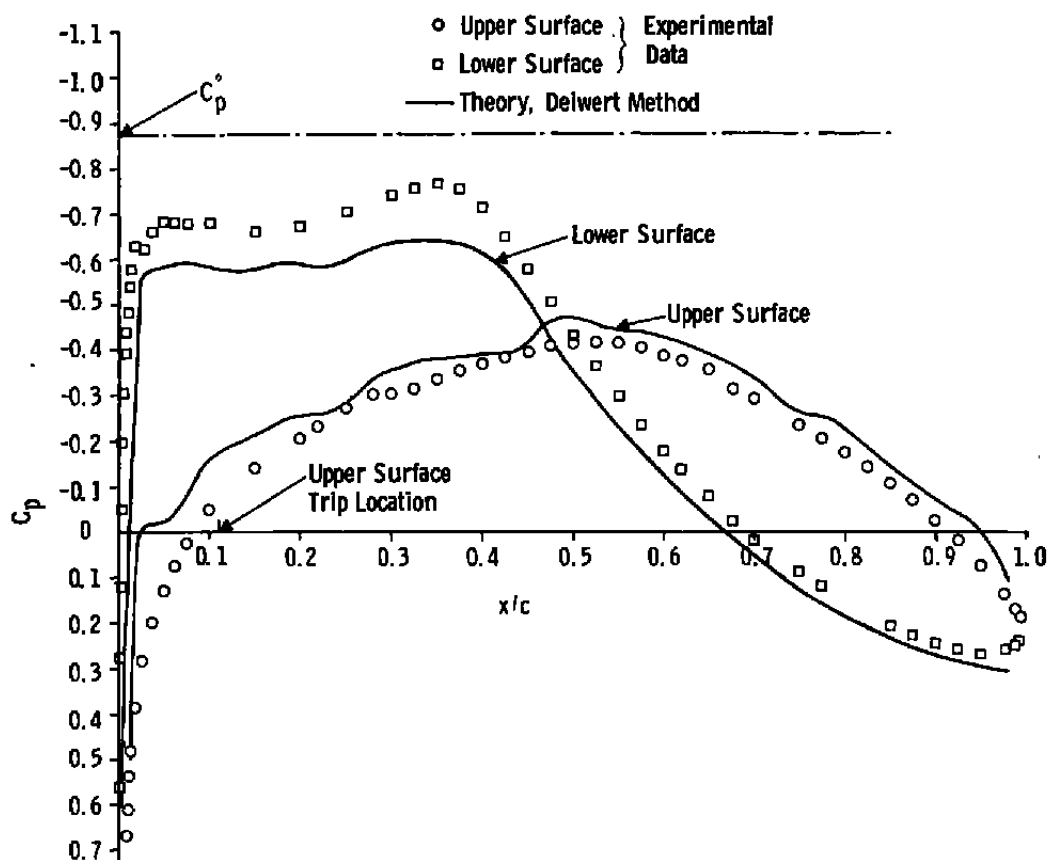
a. $M_\infty = 0.676$, $Re_{\infty,c} = 5.7 \times 10^6$, $a = -2.18$ deg (case 2)

Figure 3. Upper and lower surface pressure distributions on the RAE 2822 airfoil.
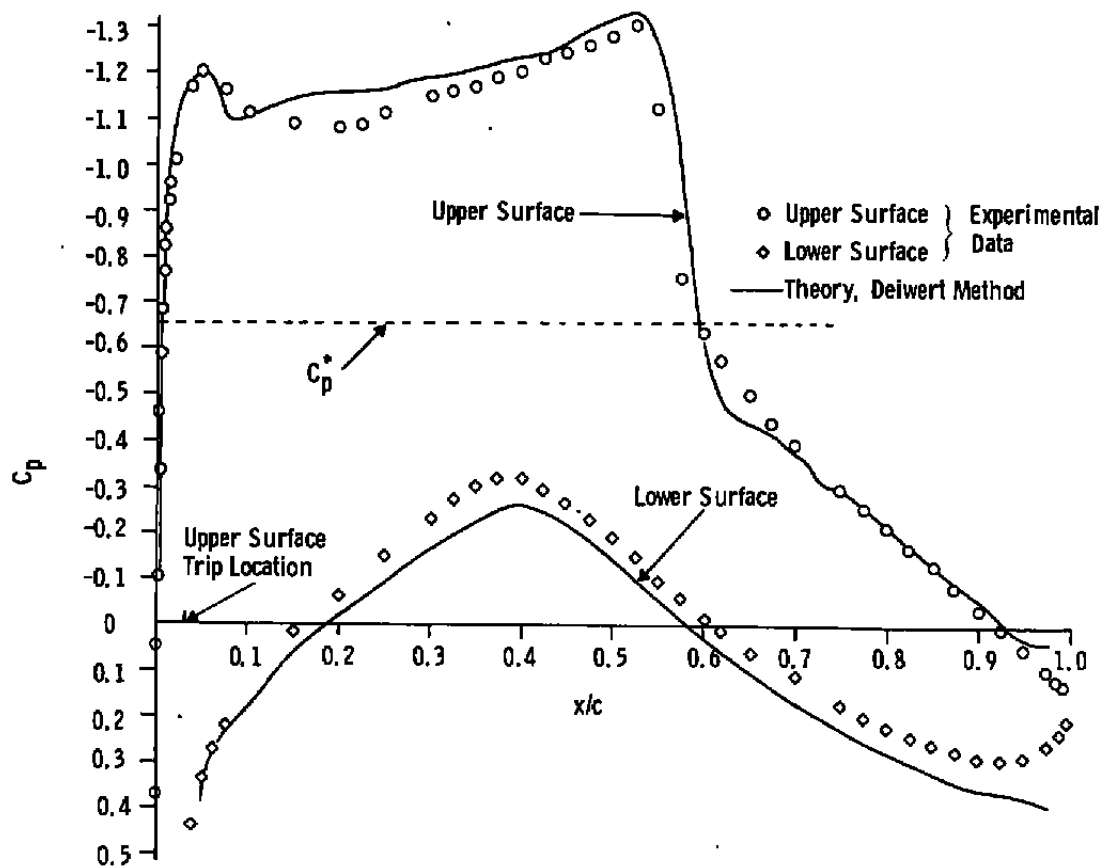
b. $M_\infty = 0.73$, $Re_{\infty,c} = 6.5 \times 10^6$, $a = 3.19$ deg (case 9)

Figure 3. Continued.

c. $M_\infty = 0.73$, $Re_{\infty,c} = 2.7 \times 10^6$, $a = 3.19$ (case 12)

Figure 3. Concluded.

21

4.1.2 Boundary-Layer Characteristics, Case 2

Results from the five calculation methods are compared with experimental skin friction data for Case 2 in Fig. 4a. The four boundary-layer calculation methods generally compare well with the experimental data. Surface skin frictions as computed by Deiwert's method are considerably higher than those measured, particularly on the downstream portion of the airfoil surface where the pressure gradient becomes adverse (Fig. 3a). However, it should be pointed out that the number of grid points within the boundary layer was at least one order of magnitude lower than those used by the boundary-layer methods which could account for the observed discrepancies in skin friction as calculated by the Deiwert program.
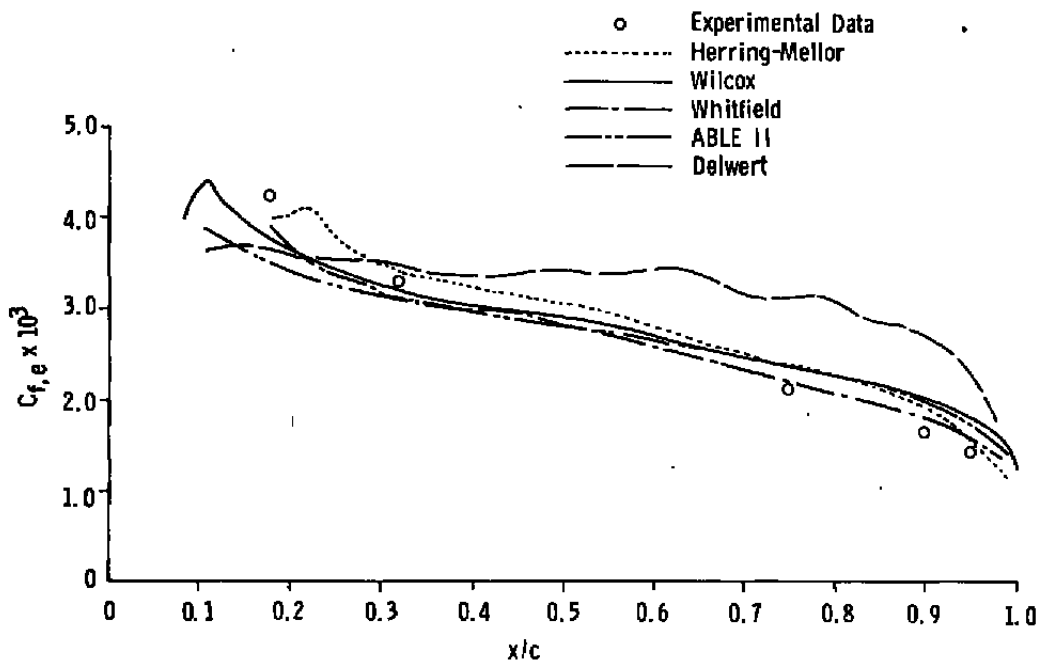

a. Skin friction

Figure 4. Upper surface boundary-layer properties of the RAE 2822 airfoil for $M_\infty = 0.676$, $Re_{\infty,c} = 5.7 \times 10^6$, $a = -2.18$ deg (case 2).

Figure 4b shows the measured and computed comparisons of upper surface boundary-layer displacement thickness (δ^*). Excellent agreement between experiment and all calculation methods exist in the upstream region where the pressure gradient is favorable. In the adverse pressure gradient region the displacement thickness increases rapdily and slightly more accurate values of δ^* are calculated by the Herring-Mellor method than any of the other boundary-layer methods. At about 70-percent chord, results as given by the Wilcox method start to deviate from the other computations and continue to calculate values of δ^* below the data for the remainder of the airfoil length.

As was noted with the airfoil surface pressure distribution calculated by the Deiwert program (Fig. 3a), the displacement thickness computed by this method exhibits oscillations downstream of 50-percent chord. It is fortuitous that the experimental data and the Deiwert computed value of displacement thickness agree at 95-percent chord.
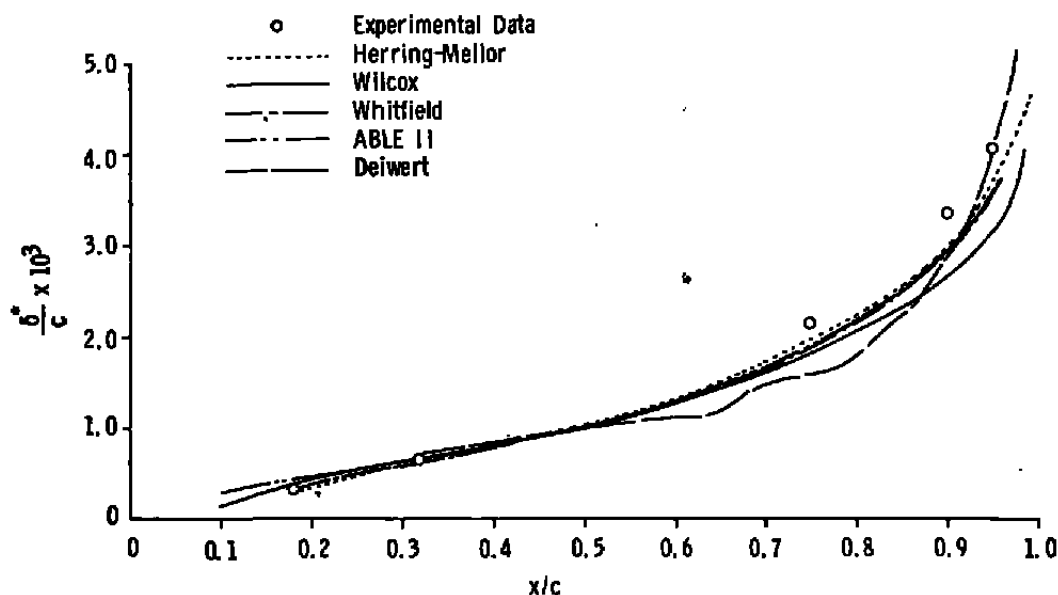

b. Displacement thickness
Figure 4. Continued.

Figure 4c illustrates better overall agreement between calculated and measured momentum thicknesses than was obtained for displacement thicknesses in Fig. 4b. Similar to the displacement thickness, the momentum thickness is seen to slowly increase in the favorable protion of the surface pressure gradient and then increases rapidly over the remaining 50 percent of the airfoil surface in the adverse pressure gradient region. The Herring-Mellor and ABLE-II methods yield good agreement with the data along the entire chord length, whereas results as computed by Whitfield and Wilcox methods are slightly under the data aft of approximately 70-percent chord. Again, results calculated by the Deiwert program contain oscillations in the solution and a significant increase in θ occurs past 90-percent chord.

Shown in Fig. 4d is the airfoil upper surface variation of the measured and computed shape factor. The data indicate almost constant values of this parameter over the first 80 percent of the airfoil chord as do the calculations by the four boundary-layer methods. Quantitatively, however, the Whitfield method shows the overall best agreement with the experimental data which may be a consequence of using the value of H at the first measuring station as input. As should be expected from Figs. 4b and c, the shape factor distribution as computed by the Deiwert method shows oscillations not found in the data or the other calculated results.
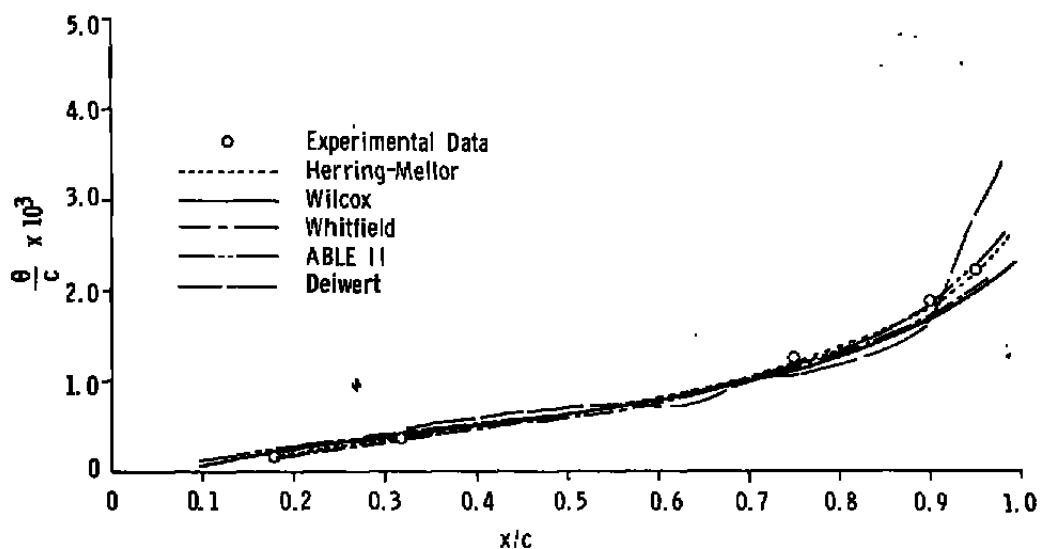
c. Momentum thickness
Figure 4. Continued.
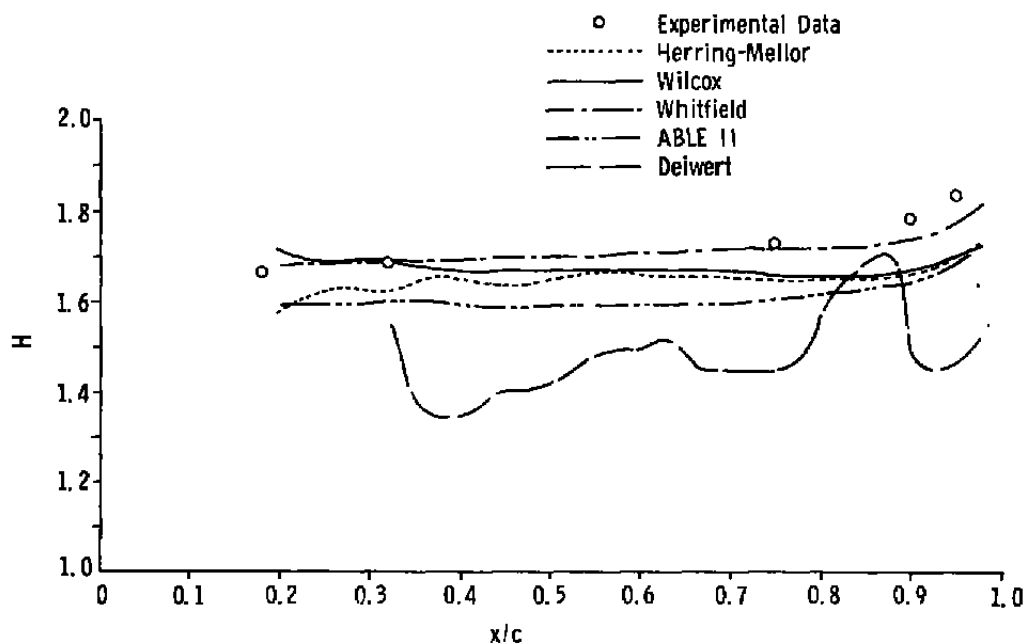
d. Shape factor
Figure 4. Concluded.

4.1.3 Boundary-Layer Characteristics, Case 9

The upper surface streamwise variation of measured and computed skin friction is shown in Fig. 5a. Upstream of the 50-percent chord position the skin friction decreases slightly with increasing x/c. Because of the presence of a shock located at about 55-percent chord and the accompanying severe compression, the experimentally determined skin friction drops significantly. All the calculation methods exhibit good qualitative trends with respect to the data. Immediately downstream of the shock at approximately 60-percent chord, all calculation methods show a decrease and then an increase in skin friction with the ABLE-II, Wilcox, and Deiwert methods showing the most severe variations. There is a slight trailing-edge separated flow region computed by the Deiwert technique which is not evident from the experimental data. Also, the ABLE-II method predicted separation at about 82-percent chord which was the only boundary-layer method to indicate such a result.
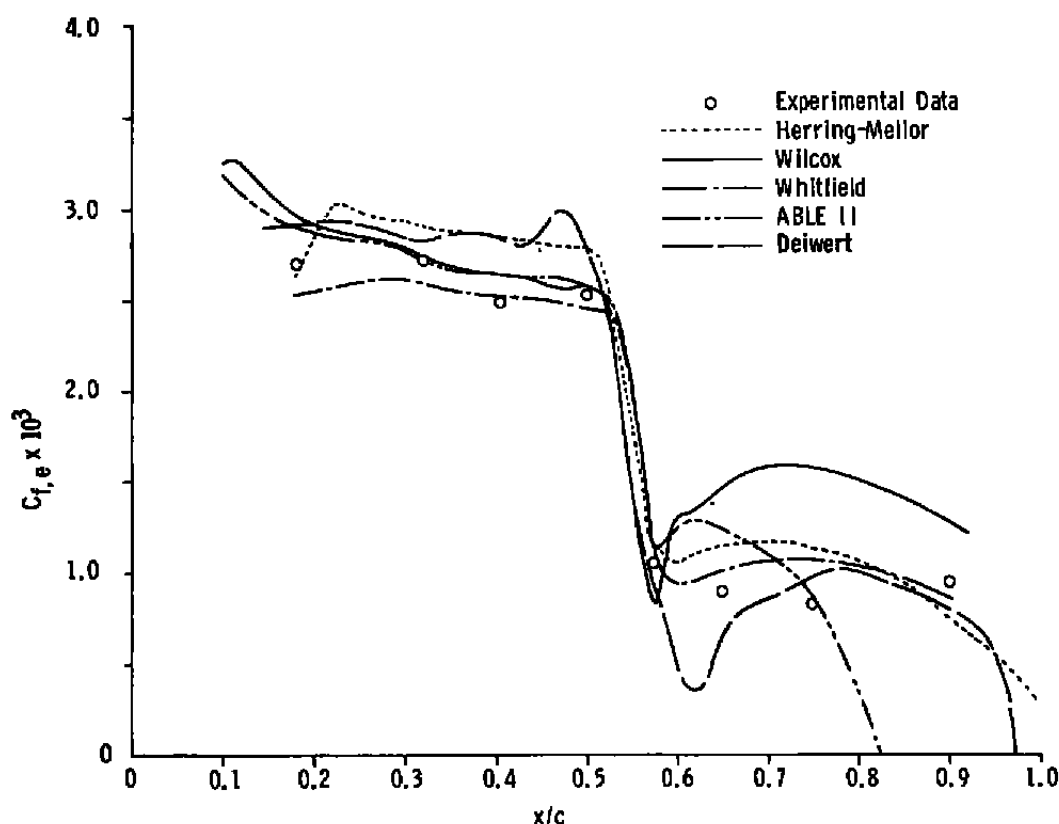

a. Skin friction

Figure 5. Upper surface boundary-layer properties of the RAE 2822 airfoil for $M_\infty = 0.73$, $Re_{\infty,c} = 6.5 \times 10^6$, $\alpha = 3.19$ deg (case 9).

The experimental and calculated variation of displacement thickness on the airfoil upper surface at the Case 9 flow conditions are shown in Fig. 5b. Upstream of the shock location (x/c = 0.55), the boundary-layer methods do a good job of calculating the values of displacement thickness, but the Deiwert method gives results that are too high. On the downstream portion of the surface, the presence of the shock and the associated severe adverse pressure gradient cause a thickening and retardation of the boundary layer, thus causing the abrupt increase in the displacement thickness. Agreement between the experiment and theory is not good at x/c > 0.6.
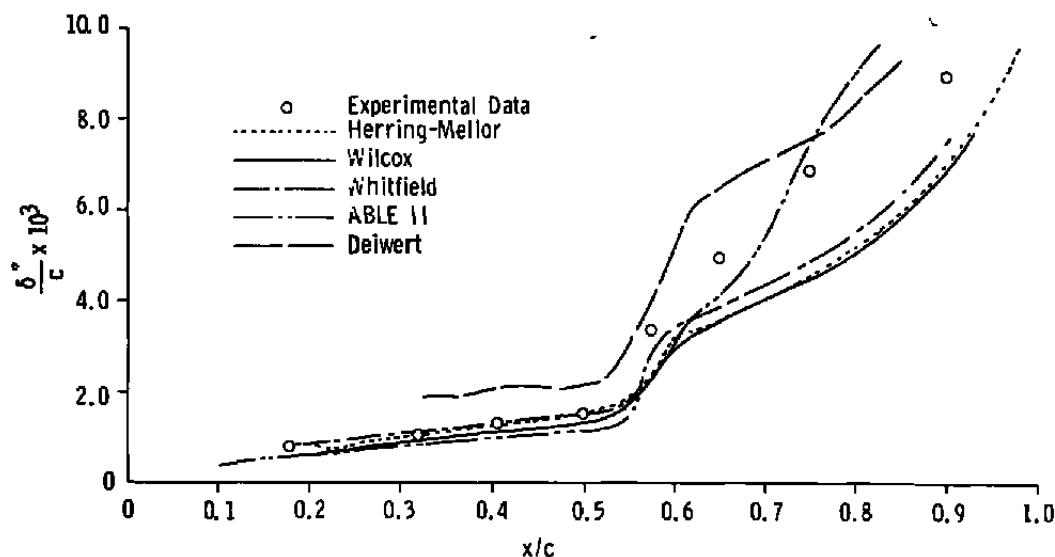
b. Displacement thickness
**Figure 5. Continued.**

Figure 5c presents the airfoil upper surface streamwise variation of momentum thickness. Upstream of the shock, the momentum thickness exhibits a gradual increase. At and downstream of the shock, a sharp increase in θ occurs. Results from the boundary-layer methods are in excellent agreement with the data upstream of the shock location, whereas the momentum thicknesses as computed by the Deiwert method in this region are too high compared with the data. Downstream of the shock, the abrupt increase in experimentally determined θ's is computed to be in close agreement to the data by the ABLE-II program; however, this method predicted separation at x/c = 0.8 which was not experimentally measured for this case. The other three boundary-layer methods yield results which lie significantly below the experimental data downstream of the shock, whereas the Deiwert method calculates momentum thicknesses which are too high but with the same rate of increase as the experimental data.

26
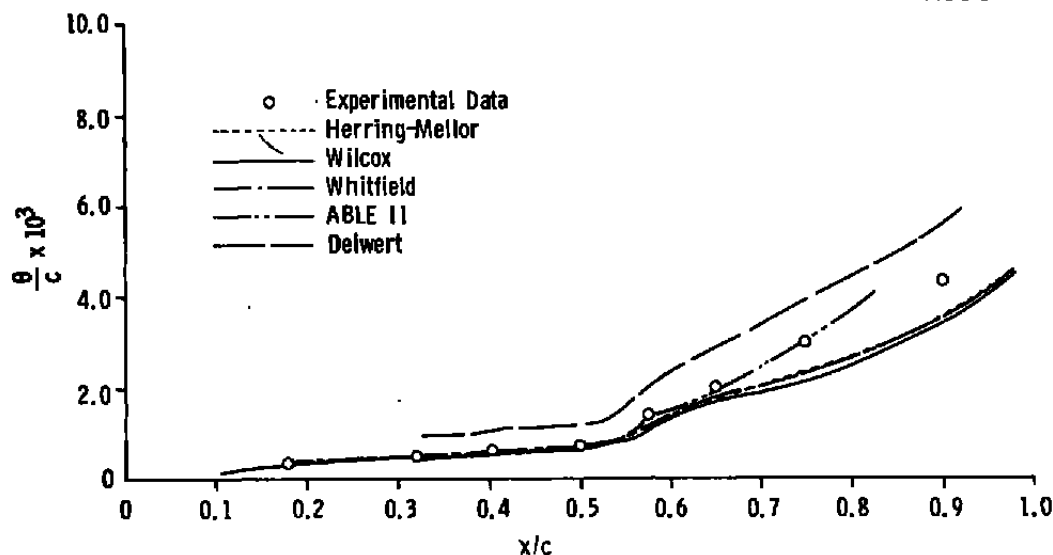
c. Momentum thickness
Figure 5. Continued.

Shown in Fig. 5d are the airfoil upper surface shape factor distributions. An abrupt increase in shape factor occurs in the shock region followed by a decrease in shape factor. This trend is qualitatively computed by all the calculation methods except the ABLE-II method. The Whitfield and Wilcox methods are in reasonably good agreement with one another along the airfoil and are in good agreement with experimental data upstream of the shock. The agreement between calculated and measured shape factors downstream of the shock is not good.
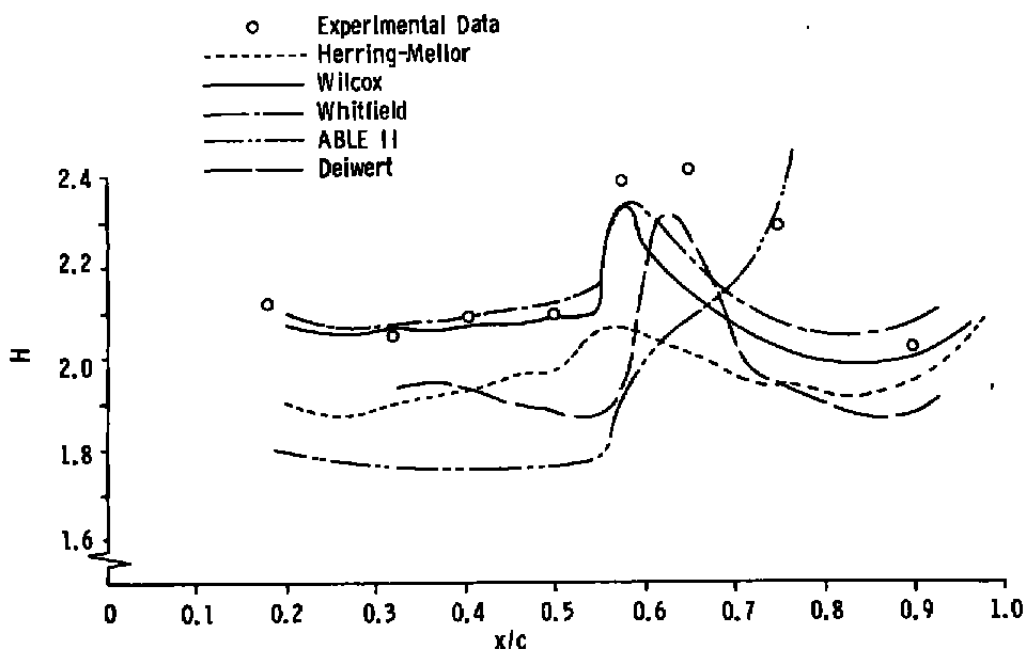

d. Shape factor
Figure 5. Concluded.

27

4.1.4 Boundary-Layer Characteristics, Case 12

For unknown reasons, the Wilcox method could not be made to run Case 12. Case 12 is similar to Case 9, except the pressure gradient is less severe and the Reynolds number is lower.

Figure 6a presents the measured and calculated skin friction on the RAE airfoil upper surface for Case 12. Unlike the higher Reynolds number case (Case 9), a more gradual decrease in surface skin friction was measured in the shock region, $0.4 \leqslant x/c \leqslant 0.7$. As with the previous two flows, no separation was indicated experimentally. Upstream of $x/c = 0.45$, the Whitfield method is in good agreement with the measured skin friction distribution, falls below that measured in the region $0.5 \leqslant x/c \leqslant 0.7$, and recovers to fair agreement over the downstream 30 percent of the airfoil surface. The Herring-Mellor method calculates values of skin friction higher than the measured data upstream of the shock, but is in good agreement with measured data in and downstream of the shock region. The ABLE-II method gives good qualitative agreement with measured data, but computes skin frictions which are higher than the measured data downstream of the shock. It is interesting to note that the ABLE-II method predicted separation at the higher Reynolds number Case 9 but not at the lower Reynolds number associated with Case 12 indicating a possible anomaly concerning this method, or the use of it. Values of skin friction calculated by the Deiwert program are too high upstream of the shock, again possibly caused by an inadequate number of grid points within the boundary-layer region. Also, because the shock location was predicted downstream of that indicated by the data (see Fig. 3c), the calculated drop in skin friction associated with the severe adverse pressure gradient is also moved downstream relative to the boundary-layer calculations. It is also noted from Fig. 6a that a small separated region was computed by the Deiwert method immediately behind the shock and also very near the airfoil trailing edge.

Figure 6b presents the streamwise variation of displacement thickness over the upper airfoil surface. Similar to the high Reynolds number case (Case 9), a slow increase in displacement thickness occurs upstream of the shock. Because of the strong adverse pressure gradient caused by the shock, a substantial increase in δ^* occurs over the aft portion of the airfoil. The boundary-layer methods calculate δ^* reasonably well except over the aft portion of the airfoil, $x/c > 0.7$. The Deiwert program does not compute the distribution of δ^* well for this case. However, it should be emphasized that the Deiwert program is concerned with computing the entire flow field, whereas the other methods treat only the boundary-layer region. The Deiwert program would require prohibitive amounts of machine storage and computation times in order to have the same numerical resolution (particularly within the boundary layer) as the boundary-layer methods.
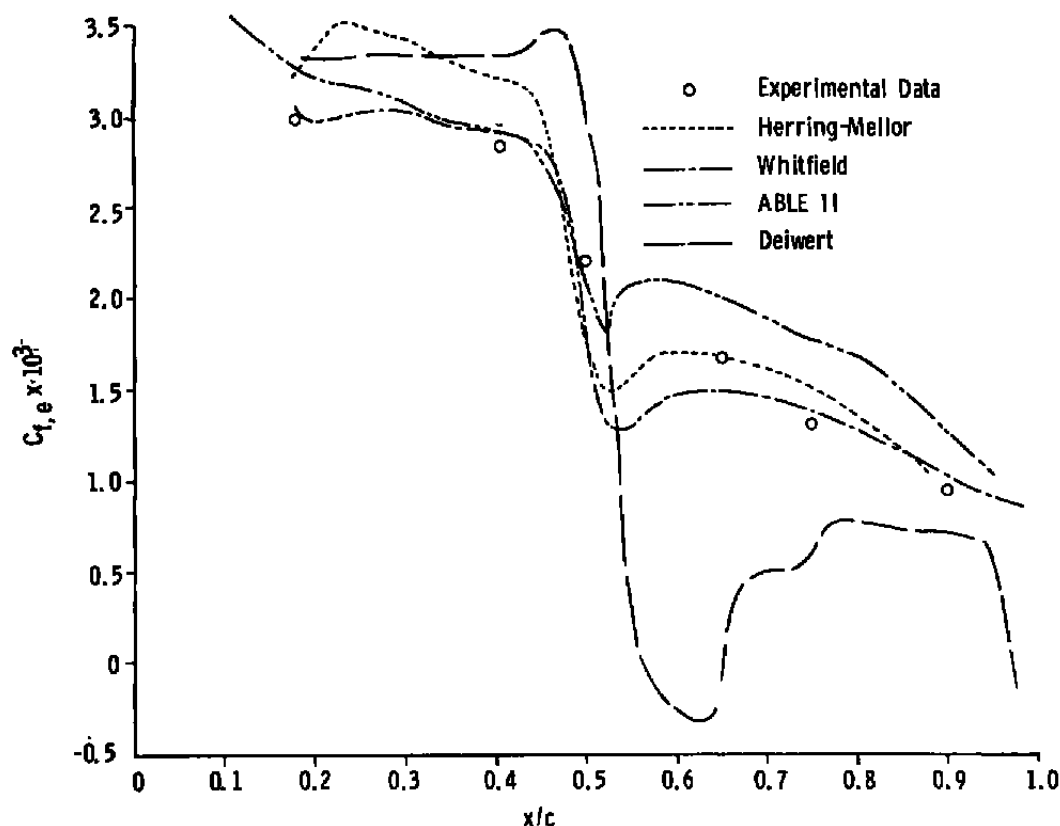
a. Skin friction
Figure 6. Upper surface boundary-layer properties of the RAE 2822 airfoil
for M_∞ = 0.73, $Re_{\infty,c}$ = 2.7 x 10^6, a = 3.19 deg (case 12).

Illustrated in Fig. 6c are the measured and computed values of momentum thickness on the airfoil upper surface at the Case 12 flow conditions. All of the boundary-layer calculation methods give results which agree reasonably well with measured data. Si nilar to the results for Cases 2 and 9, these results indicate that the boundary-layer methods do a better job of predicting momentum thickness than they do displacement thickness.

Figure 6d shows the experimental and computed airfoil upper surface shape factor distributions for the Case 12 flow conditions. Unfortunately, there are insufficient experimental data to resolve the region where the predictions indicate a peak in H. The Whitfield method gives good agreement upstream of the shock primarily because H is an initial condition. Downstream of the shock the ABLE-II method gives the best qualitative agreement with measured data, but the quantitative agreement is not particularly good.
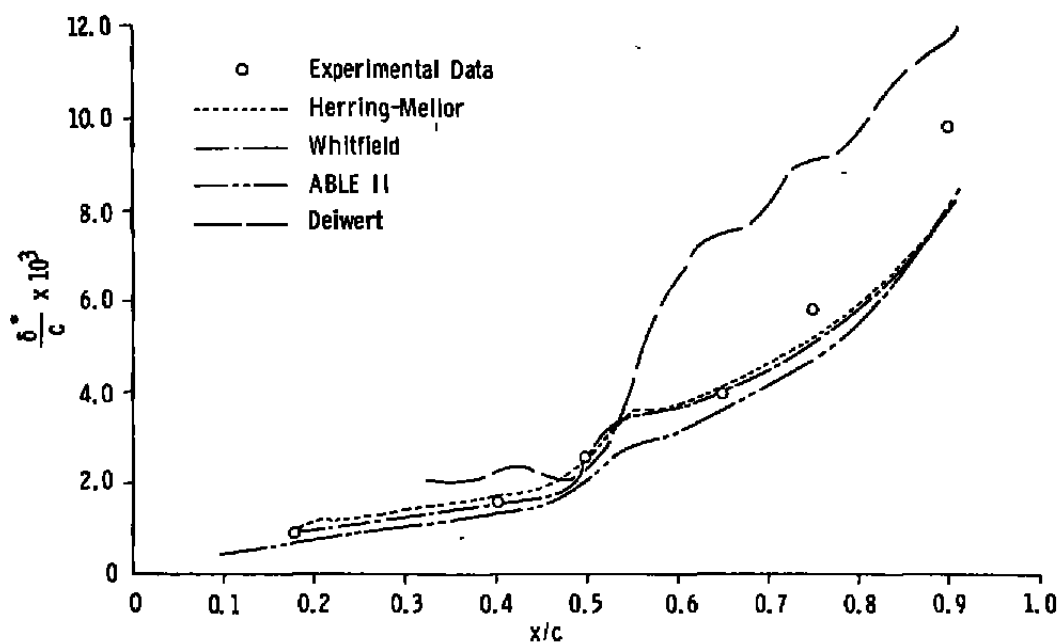
b. Displacement thickness
Figure 6. Continued.
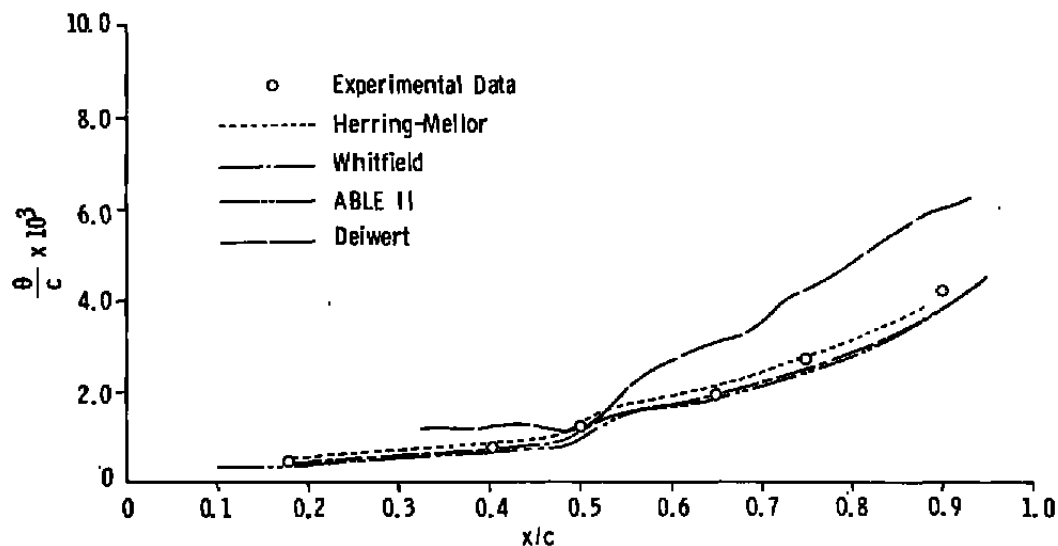
c. Momentum thickness
Figure 6. Continued.
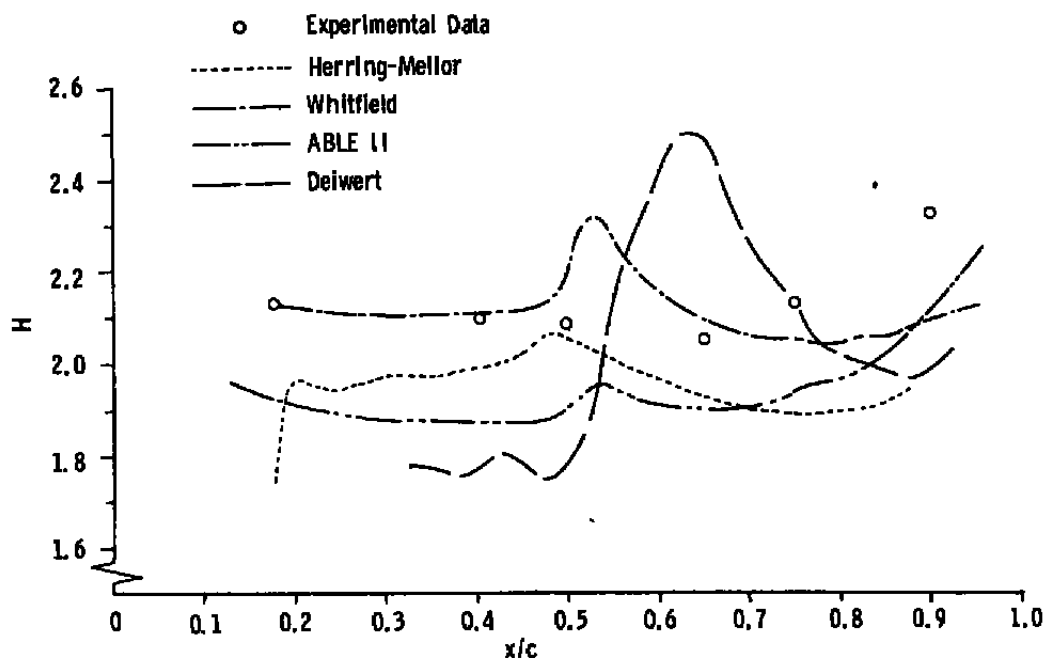
d. Shape factor
Figure 6. Concluded.

Shown in Table 2 are comparisons of calculated results on the RAE airfoil in the form of qualitative judgements as to which calculation method gave the most accurate predictions for each boundary-layer property examined. The "X's" represent a choice of the most accurate method while the "O's" signify the method is slightly less accurate than the most accurate method.

Table 2 illustrates that the Whitfield method gave the most accurate skin frictions for Cases 9 and 12 (supercritical). The Herring-Mellor program predicted the most accurate skin frictions for Case 2 (subcritical). Overall, equal accuracy was achieved between the Whitfield and Herring-Mellor methods. However, the fact that both the Whitfield and Herring-Mellor solutions were started from initial conditions at the first measuring station, and the ABLE-II and Wilcox solutions were started upstream of this point with initial conditions such that the momentum thickness of the first measuring station was approximately matched, could influence how well these methods agreed with experimental data downstream of this point. Unfortunately, solutions could not be obtained from all methods which satisfied the same set of initial conditions, which of course, would be the basis for proper comparison.

31

Table 2. Relative Accuracy of the Computational Methods for the
RAE Airfoil Comparisons

Method	Case 2				Case 9				Case 12			
	$C_{f,e}$	$\delta*$	θ	H	C_{fe}	$\delta*$	C	H	C_{fe}	$\delta*$	θ	H
Whitfield	0	-	-	X	X	X	0	X	X	0	0	X
Herring-Mellor	X	X	X	-	0	0	X	-	0	X	X	-
ABLE II	-	0	0	-	-	-	-	-	0	-	-	-
Wilcox	-	-	-	-	-	-	-	0	*	*	*	*
Deiwert	-	-	-	-	-	-	-	-	-	-	-	-
Figure	4a	b	c	d	5a	b	c	d	6a	b	c·	d

Legend:　X　Judged to be most accurate method

　　　　　O　Judged to be slightly less accurate then above

　　　　　-　Judged to be significantly less accurate than either of the above

　　　　　*　Wilcox method could not be made to compute this flow

4.2 WAISTED BODY OF REVOLUTION

The waisted body of revolution model used for the experiments reported in Ref. 2 was designed such that an axisymmetric, converging flow with an adverse pressure gradient could be produced and the effect of Mach number, pressure gradient, and streamline convergence and divergence on the turbulent boundary layer could be investigated. Two sets of experimental data taken on the waisted body of revolution were selected for comparisons with the boundary-layer solutions: a subsonic case with M_∞ = 0.597, $Re_{\infty,L}$ = 9.98 x 10^6, and a supersonic case with M_∞ = 1.398, $Re_{\infty,L}$ = 10.08 x 10^6. The Deiwert method used could compute only planar flows.

Figure 7 shows the surface pressure distributions at the two selected flow conditions. The distribution of pressures upstream of the body waist (x/L = 0.7) are similar for the two Mach numbers considered in that strong favorable and adverse pressure gradients are produced in both cases. However, downstream of the waist the subsonic flow tends to re-expand, whereas the supersonic case initially begins to expand and then recompresses over the final protion of the body.
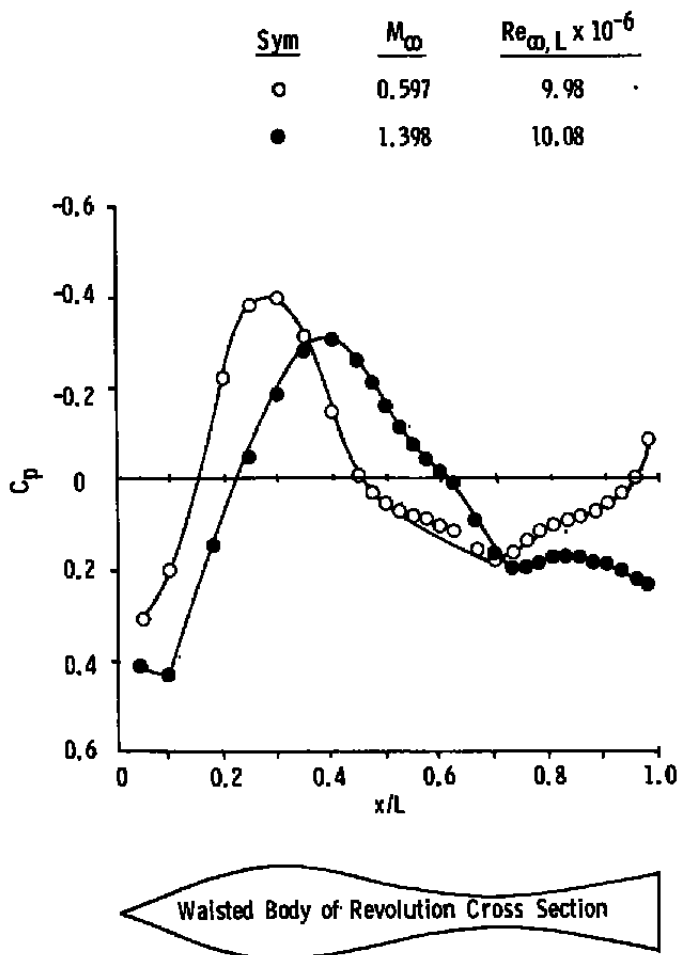
Sym	M_∞	$Re_{\infty, L} \times 10^{-6}$
o	0.597	9.98
●	1.398	10.08

Figure 7. Pressure distributions on the waisted body of revolution.

4.2.1 Subsonic

Illustrated in Fig. 8a are the measured and computed body surface skin friction distributions for the case in Fig. 7 denoted by the open symbols. In the region $0.3 \leqslant x/L \leqslant 0.7$, the adverse pressure gradient coupled with the flow convergence associated with the thinning of the body produces a generally decreasing $C_{f,e}$ with the minimum value occurring near the body waist. The favorable pressure gradient aft of $x/L = 0.7$ promotes an increase in the measured skin friction. All four calculation methods give results that compare favorably with the experimental data in terms of qualitative trends, although all methods quantitatively compute values of skin friction higher than the data. The Whitfield method yields the best agreement with the experimental data. The values of skin friction computed by the Wilcox program are high over most of the body but drop to near that measured in the waist region. In the region $0.4 \leqslant x/L \leqslant 0.55$, the values of

33

skin friction as calculated by the Herring-Mellor program are increasing, whereas the other calculations (and also the experimental data) show the opposite trend. It is interesting to note that although the Whitfield method yields the best agreement with these experimental data, the transverse curvature terms in the equations are neglected in this analysis. However, the maximum value of δ^*/r_w is about 0.16 and hence the effect of transverse curvature should not be too significant for these flow conditions. The sensitivity of the Whitfield method to initial conditions is illustrated in Fig. 21 of Ref. 3 for these experimental data. Four sets of initial conditions were used in Ref. 3. All four solutions rapidly converge, indicating little sensitivity to initial conditions for these flow conditions.
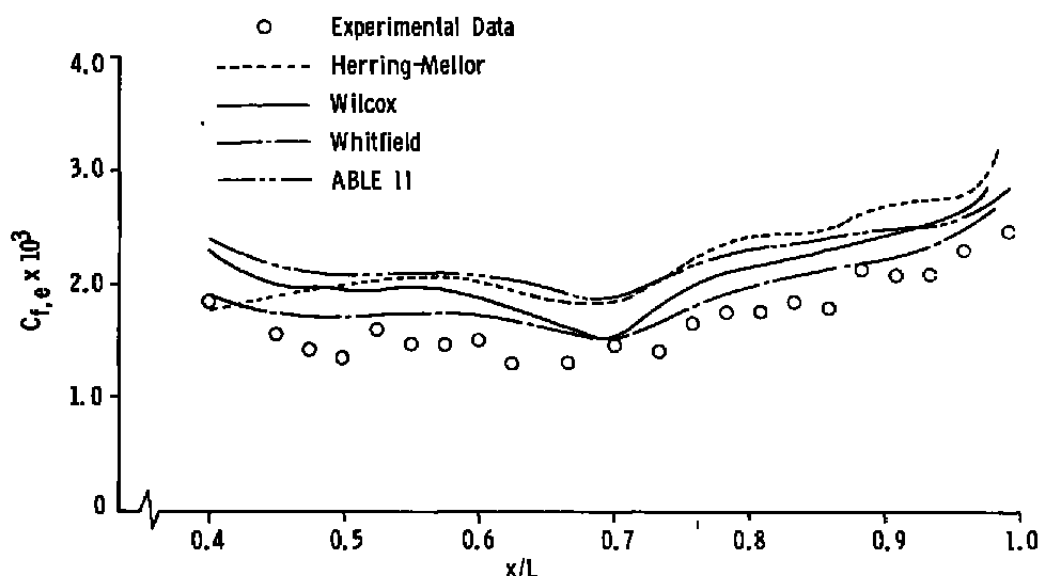
a. Skin friction
Figure 8. Boundary-layer properties on the waisted body of revolution for $M_\infty = 0.597$, $Re_{\infty,L} = 9.98 \times 10^6$.

Figure 8b presents the distribution of displacement thickness variations at the subsonic flow conditions. In the region $0.4 \leq x/L \leq 0.7$, the flow convergence and adverse pressure gradient promote a rapid thickening of the boundary layer and an accompanying increase in the displacement thickness. Over the last 30 percent of the body, the flow divergence along with the favorable pressure gradient produce a thinning of the boundary layer along with a decrease in the displacement thickness. Generally, good agreement between measured and calculated values of δ^* is obtained over the entire body with the Whitfield method possibly yielding the best results. The maximum value of δ^* located at the waist is calculated well by the Herring-Mellor method which computes values of displacement thickness higher than the data elsewhere.
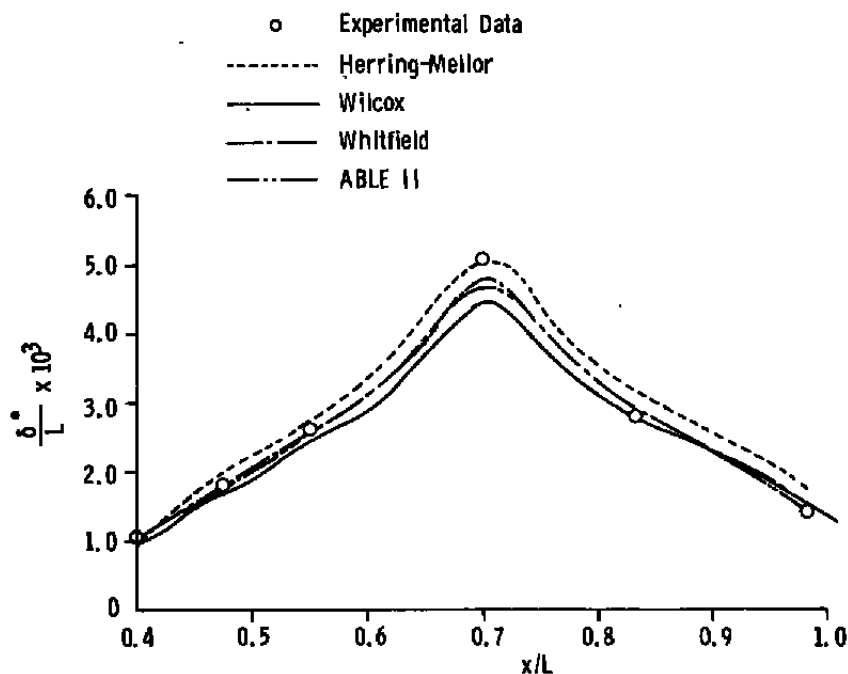
b. Displacement thickness
Figure 8. Continued.

The measured and computed axial variations of momentum thickness are shown in Fig. 8c. The experimental data exhibit the same increasing-decreasing trend as the displacement thickness distribution (Fig. 8b) which corresponds to the successive flow convergence-divergence and the adverse-favorable pressure gradient effects. The Herring-Mellor program calculates values of momentum thickness significantly higher than the measured values of momentum thickness over the entire body length. For this particular case, results computed by the ABLE-II and Whitfield methods show good agreement with the experimental data. Values of θ as computed by the Wilcox program are generally lower than the experimental data.

Figure 8d gives the calculated and experimentally determined streamwise variation of shape factor at the subsonic flow conditions. Values of boundary-layer shape factor calculated by the Whitfield program show fairly good agreement with the data, whereas the remaining three methods yield a wide disparity of shape factor distributions as compared to the experimental data (recall that H and θ are inputs to the Whitfield program).
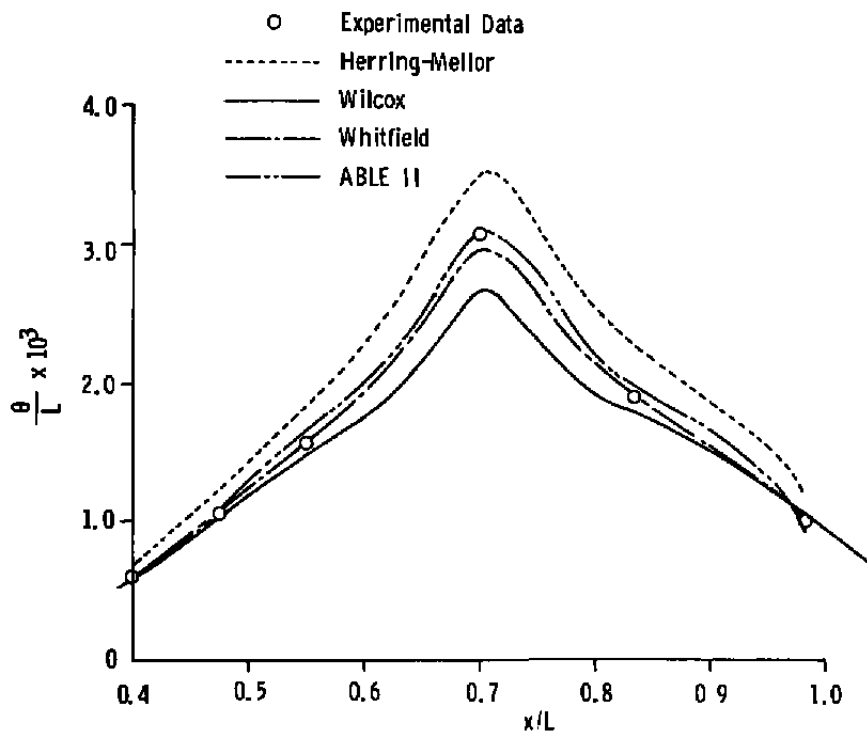
c. Momentum thickness
Figure 8. Continued.
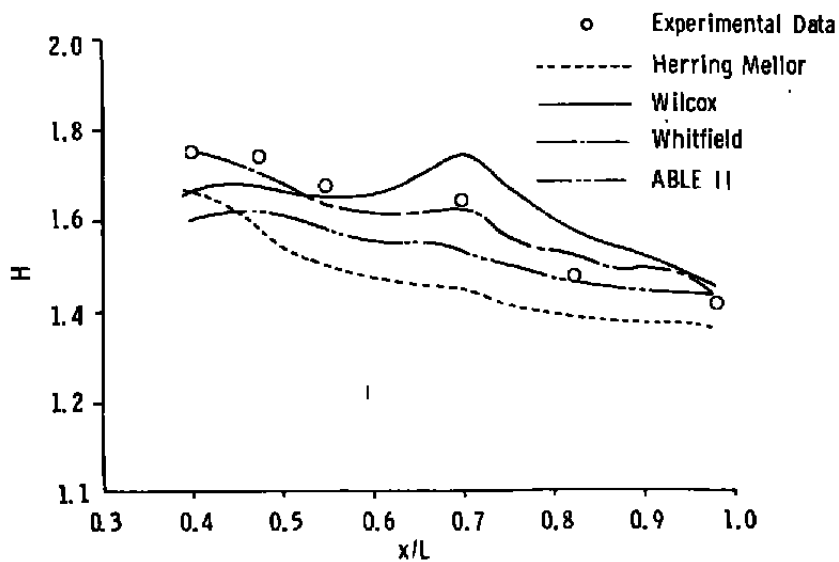
d. Shape factor
Figure 8. Concluded.
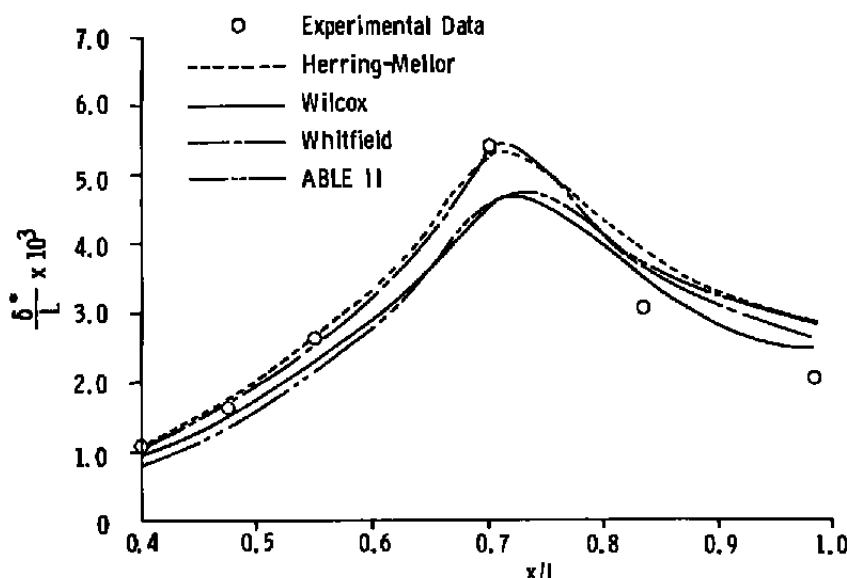
4.2.2 Supersonic

The streamwise variation of surface skin friction for the supersonic flow conditions as measured and calculated is shown in Fig. 9a. Similar to the subsonic case, flow convergence along with the adverse pressure gradient in the region $0.4 \leqslant x/L \leqslant 0.7$ produce a gradual decrease in measured values of surface skin friction; the minimum value again occurs near the body waist. Downstream of the waist, the flow diverges as the body diameter increases and there is an increase in the measured values of surface skin friction. Upstream of the body waist ($x/L = 0.7$), the computations are generally too high compared to that which was measured. However, values of $C_{f,e}$ computed by the Whitfield method are in better agreement with the data than are the other three calculation techniques. Downstream of the body waist, the Whitfield method computed values of $C_{f,e}$ which eventually fall below those measured, whereas the other three methods all yield skin frictions which are higher than those experimentally determined except near the end of the body. Over the last ten percent of the body, however, the Herring-Mellor, ABLE-II, and Wilcox programs all calculate skin frictions close to the experimental data, whereas those computed by the Whitfield method are low. However, a compatibility check performed by Winter, Rotta, and Smith (Ref. 2), which consisted of using measured values of $C_{f,e}$ and H in the momentum equation, led them to the conclusion that the skin friction was too large for $x/L > 0.7$. They attributed this to the technique used to measure skin friction (Ref. 31).
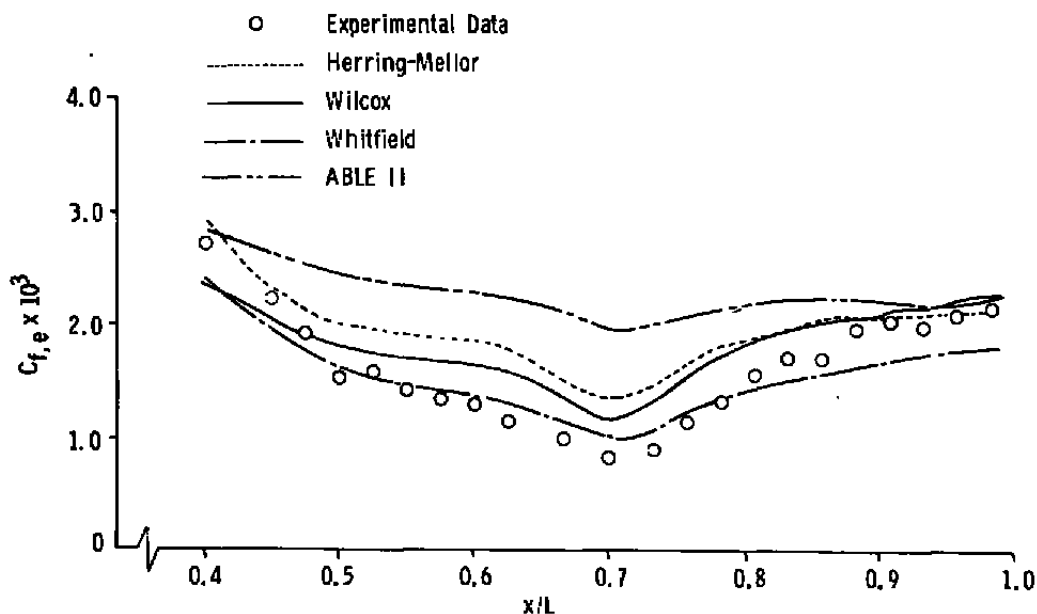
a. Skin friction
Figure 9. Boundary-layer properties on the waisted body of revolution for $M_\infty = 1.398$, $Re_{\infty,L} = 10.08 \times 10^6$.

Figure 9b shows the measured and calculated displacement thickness distribution over the body at the supersonic flow conditions. The thickening of the boundary layer enhanced by flow convergence and an adverse pressure gradient upstream of the body waist reflect a corresponding increase in the measured values of δ^*, the maximum of which occurs again near the waist of the body. Downstream of this location, divergence of the flow thins the boundary layer. General trends are predicted well by all four methods, but upstream of the body waist, values of δ^* calculated by Whitfield and Herring-Mellor methods are in better agreement with the data than either of the other methods. Downstream of the body waist, all four calculation methods compute values of δ^* higher than the data.

b. Displacement thickness
Figure 9. Continued.

Shown in Fig. 9c are the values of momentum thickness at the supersonic flow conditions. Upstream of $x/L = 0.7$ (body waist), the Herring-Mellor method tends to compute values of θ which are too high, whereas those calculated by the Wilcox program are too low. In this same region, the Whitfield and ABLE-II methods calculate values of momentum thickness which are in better agreement with the experimental data. Downstream of the body waist, the Herring-Mellor, ABLE-II, and Whitfield methods give values of θ higher than those actually measured. In this region, the Wilcox program more accurately computes the correct quantitative values of the momentum thickness.

The axial distribution of boundary-layer shape factor as measured and computed at the supersonic flow conditions are shown in Fig. 9d. In this case, the Whitfield and Wilcox methods give the best descriptions of the shape factor distribution upstream of

the body waist (x/L = 0.7). Aft of x/L = 0.7, shape factors computed by the Whitfield and Wilcox methods are too high, whereas those calculated by the Herring-Mellor and Able-II methods are in better agreement with the experimental data.
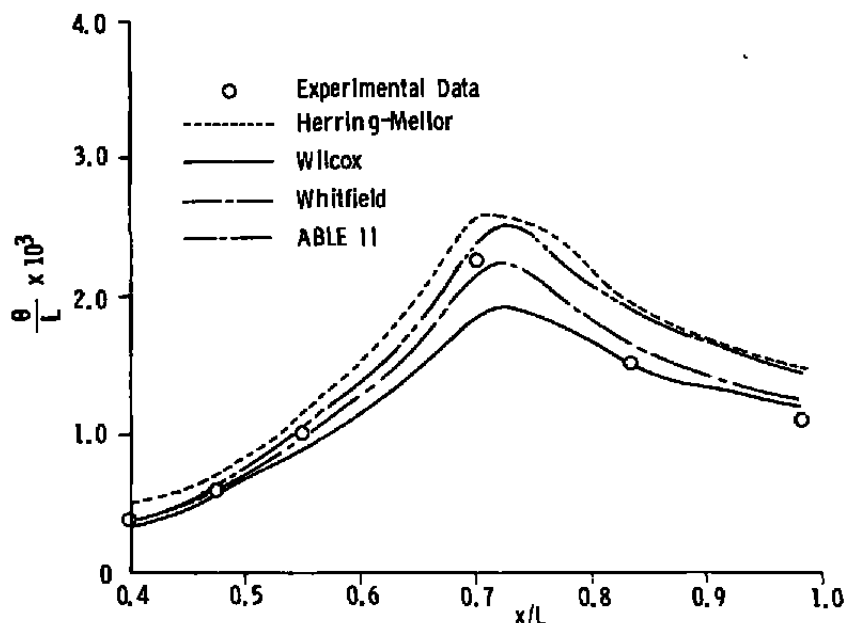
c. Momentum thickness
Figure 9. Continued.
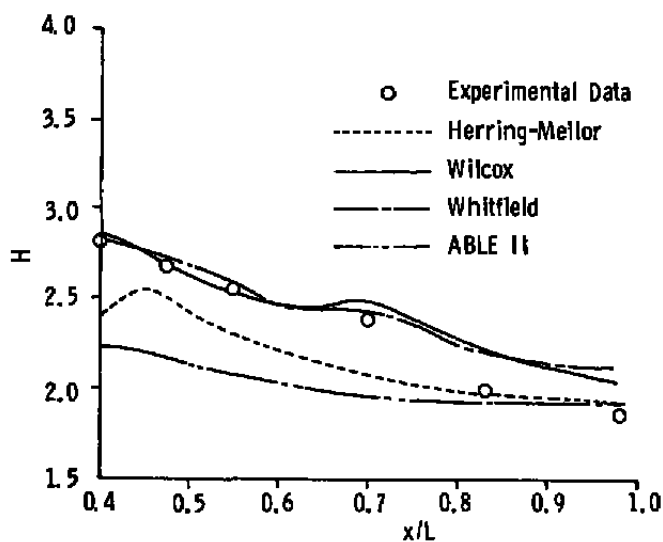
d. Shape factor
Figure 9. Concluded.

· Table 3 presents qualitative results as to which technique was judged to yield the most accurate boundary-layer calculations using the experimental data as the standard of accuracy. In both the subsonic and supersonic cases, the Whitfield method gave the most accurate computations of skin friction. For these cases, the Whitfield program also more accurately calculated almost all of the boundary-layer integral properties. However, the same caution offered in Section 4.1.4 concerning initial conditions applies here. Therefore, the conclusions are applicable only to the particular experimental data used for comparison, and the manner in which initial conditions were implemented for each calculation procedure.

Table 3. Relative Accuracy of the Computational Methods for the Waisted Body of Revolution Comparisons

Method	Subsonic				Supersonic			
	$C_{f,e}$	$\delta*$	θ	H	C_{fe}	$\delta*$	θ	H
Whitfield	X	X	X	X	X	X	X	0
Herring-Mellor	–	0	–	–	–	0	–	–
ABLE II	–	0	0	–	–	–	0	–
Wilcox	0	–	–	–	0	–	0	X
Figure	8a	b	c	d	9a	b	c	d

```
Legend:  X   Judged to be the most accurate method

         0   Judged to be slightly less accurate than above

         -   Judged to be significantly less accurate than
             either of the above
```

5.0 CONCLUSIONS

Numerical calculations have been made to determine the accuracy of five computer programs to compute the skin friction on a two-dimensional wing and a body of revolution in transonic flow. It was shown that of the five computational methods considered, the integral boundary-layer method by Whitfield and the finite difference boundary-layer method of Herring and Mellor with algebraic turbulence modeling provided the best agreement with the nonseparated, transonic, adiabatic wall data considered. These methods were also the most simple to use and required less computer

resources than the other methods considered. This result, however, must be tempered by the fact that all calculation procedures did not require and could not be started with identical initial conditions.

REFERENCES

1. Cook, P. H., McDonald, M. A., and Firmin, M.C.P. "Aerofoil RAE 2822 — Pressure Distributions, Boundary Layer and Wake Measurements." Royal Aircraft Establishment, UK, AGARD WG 04, July 1977.

2. Winter, K. G., Rotta, J. C., and Smith, K. G. "Studies of the Turbulent Boundary Layer on a Waisted Body of Revolution in Subsonic and Supersonic Flow." Aeronautical Research Council, Reports and Memoranda No. 3633, August 1968.

3. Whitfield, D. L. "Integral Solution of Compressible Turbulent Boundary Layers Using Improved Velocity Profiles." AEDC-TR-78-42, 1978.

4. Whitfield, D. L. "Analytical Description of the Complete Turbulent Boundary-Layer Velocity Profile." AIAA Paper No. 78-1158, July 1978.

5. Whitfield, D. L. and High, M. D. "Velocity-Temperature Relations in Turbulent Boundary Layers with Nonunity Prandtl Numbers." AIAA Journal, Vol. 15, No. 3, March 1977, pp. 431-434.

6. Hinze, J. O. Turbulence. Second Edition, McGraw-Hill, Inc., New York, 1975.

7. Clauser, F. H. "The Turbulent Boundary Layer." Advances in Applied Mechanics. Vol. 4, New York, 1956, pp. 1-51.

8. Nash, J. F. "A Practical Calculation Method for Compressible Turbulent Boundary Layers in Two-Dimensional and Axisymmetric Flows." Lockheed-Georgia Company, Research Memorandum-ER-9428, August 1967.

9. Herring, H. J. and Mellor, G. L. "A Method of Calculating Compressible Turbulent Boundary Layers." NASA CR-1144, September 1968.

10. Herring, H. J. and Mellor, G. L. "Computer Program for Calculating Laminar and Turbulent Boundary Layer Development in Compressible Flow." NASA CR-2068, June 1972.

11. Mellor, G. L. and Gibson, D. M. "Equilibrium Turbulent Boundary Layers." Journal of Fluid Mechanics, Vol. 24, 225-253, 1966.

12. Probstein, R. E. and Elliot, D. "The Transverse Curvature Effect in Compressible Axially Symmetric Laminar Boundary-Layer Flow." Journal of the Aeronautical Sciences, Vol. 23, No. 3, 1956, pp. 208-224, Concluded on p. 236.

13. Mellor, G. L. and Herring, H. J. "Two Methods of Calculating Turbulent Boundary-Layer Behavior Based on Numerical Solutions of the Equations of Motion." Proceedings - Conference on Computation of Turbulent Boundary Layer Prediction. Stanford University, 1968.

14. Patankar, S. V. and Spalding, D. B. Heat and Mass Transfer in Boundary Layers. 2nd Edition, Intertext Books, 1970.

15. Whitfield, D. L. "Analytical, Numerical, and Experimental Results on Turbulent Boundary Layers." AEDC-TR-76-62 (ADA027588), July 1976.

16. Wilcox, D. C. "User's Guide for the EDDYBL Computer Program." DCW Industries, Sherman Oaks, California, November 1976.

17. Hayes, W. D. and Probstein, R. F. Hypersonic Flow Theory. Academic Press, 1959, p. 290.

18. Flugge-Lotz, I. and Blottner, F. G. "Computation of the Compressible Laminar Boundary-Layer Flow Including Displacement-Thickness Interaction Using Finite-Difference Methods." AFOSR 2206, January 1962.

19. Deiwert, G. S. "Numerical Simulation of High Reynolds Number Transonic Flows." AIAA Paper No. 74-603, Palo Alto, California, June 1974.

20. Deiwert, G. S. "Mixed Finite Differences Approach for Compressible Navier-Stokes Equations and Turbulence Modeling in Navier-Stokes Simulations." Lecture Notes for Short Course on Advances in Computational Fluid Dynamics, The University of Tennessee Space Institute, Tullahoma, Tennessee. December 5-9, 1977.

21. Deiwert, G. S. "High Reynolds Number Transonic Flow Simulation." Lecture Notes in Physics, Vol. 35, Springer-Verlag, 1975.

22. Cebecci. T. and Smith, A.M.O. Analysis of Turbulent Boundary Layers. Academic Press, New York, N. Y., 1974.

23. Rubesin, M. W. and Rose, W. C. "The Turbulent Mean-Flow, Reynolds-Stress, and Heat-Flux Equations in Mass-Averaged Dependent Variables." NASA TMX-62,248, March 1973.

24. MacCormack, R. W. "An Efficient Numerical Method for Solving the Time-Dependent Compressible Navier-Stokes Equations at High Reynolds Numbers." NASA TMX-73,129, July 1976.

25. MacCormack, R. W. "The Effect of Viscosity in Hypervelocity Impact Cratering." AIAA Paper No. 69-354, April 1969.

26. MacCormack, R. W. "Numerical Methods for Hyperbolic Systems." Lecture Notes for Short Course on Advances in Computational Fluid Dynamics, The University of Tennessee Space Institute, Tullahoma, Tennessee, December 10-14, 1973.

27. Liepmann, H. W. and Roshko, A. Elements of Gasdynamics. John Wiley and Sons, New York, N. Y., 1957, p. 337.

28. MacCormack, R. W. and Baldwin, B. S. "A Numerical Method for Solving the Navier-Stokes Equations with Application to Shock-Boundary Layer Interactions." AIAA Paper No. 75-1, 1975.

29. Winter, K. G. and Gaudet, L. "Turbulent Boundary-Layer Studies at High Reynolds Number at Mach Numbers Between 0.2 and 2.8." ARC R&M 3712, December 1970.

30. Myring, D. F. "The Effects of Normal Pressure Gradients on the Boundary Layer Momentum Integral Equation." RAE Technical Report 68214, August 1968.

31. Smith, G. G., Gaudet, L., and Winter, K. G. "The Use of Surface Pitot Tubes as Skin Friction Meters at Supersonic Speeds." Aeronautical Research Council, Reports and Memoranda No. 3351, June 1962.

32. Rubesin, M. W., Okuno, A. F., Mateer, G. G., and Brash, A. "Flush-Mounted Hot-Wire Gage for Skin Friction and Separation Detection Measurements." Paper presented at International Conference on Instrumentation in Aerospace Simulation Facilities, Canadian Government Conference Center, Ottawa, Canada, September 22-24, 1975.

NOMENCLATURE

c   Airfoil chord; also $[3.1 - 1.82 \, Re_{\infty,x} \times 10^6]$ used in Eq. (25)

$C_{f,e}$ Local skin friction coefficient based on boundary-layer edge conditions, $2\tau_w / \rho_e u_e{}^2$

c_p Specific heat

C_p Pressure coefficient $= 2(p - p_\infty)/\rho_\infty U_\infty{}^2$

C_p^* Critical pressure coefficient

D   Dissipation integral, Eq. (5)

e   Turbulent kinetic energy (TKE) per unit mass

e_i Local mean internal energy

e_t Local mean total energy, $\rho[e_i + (u^2 + v^2)/2]$

$\vec{e}_x, \vec{e}_y$ Unit vectors in the x and y directions, respectively

h   Local mean fluid enthalpy, $e_i + p/\rho$

H   Local boundary-layer shape factor, δ^*/θ

$\vec{H}$ Column vector defined by Eq. (35)

k   Local mean thermal conductivity; also exponent governing whether flow is taken to be planar (k = 0) or axisymmetric (k = 1)

ℓ Mixing length, Eqs. (42) and (43)

L   Length of body; also dissipation length used in Eq. (25)

M   Mach number

$\vec{n}$ Unit vector normal to a grid cell face

p   Local mean pressure

Pr   Prandtl number

Pr_t Turbulent Prandtl number

q	Local mean heat flux
r	Transverse wall radius for axisymmetric flow
$\tilde{R}$	Local Reynolds number defined by Eq. (17)
Re	Reynolds number, $\rho u s/\mu$
R_s	Longitudinal radius of curvature of surface used in Eqs. (32) and (33)
S	Length variable
t	Time
T	Local mean temperature
u	Local mean fluid velocity component parallel to body surface
U	Column vector defined in Eq. (35)
U_e	Local mean boundary-layer-edge velocity
v	Local mean fluid velocity component normal to body surface
$\vec{V}$	Local mean velocity vector, $u\vec{e}_x + v\vec{e}_y$
x	Axial or streamwise coordinate
y	Coordinate normal to body surface
y^+	Law-of-the-wall coordinate, $y\sqrt{\tau_w \rho_w}/\mu_w$
α	Airfoil angle of attack; also variable used in Eq. (33)
α^*	Variable used in Eq. (32)
α_{ef}	Local mean effective thermal conductivity defined by Eq. (15)
β	Angle between tangent to body surface and free-stream velocity vector, Eq. (24); also constant used in Eq. (33)
β^*	Constant used in Eq. (33)
δ	Local boundary-layer thickness

δ^*	Local boundary-layer displacement thickness
δ^{**}	Defined by Eq. (3)
$\overline{\delta}^*$	Incompressible displacement thickness, Eq. (8)
$\tilde{\delta}^*$	Local boundary-layer displacement thickness which includes body radius term, Eq. (44)
ϵ	Eddy viscosity; also eddy diffusivity, Eqs. (29 through 33)
θ	Local boundary-layer momentum thickness
θ^*	Defined by Eq. (4)
$\tilde{\theta}$	Local boundary-layer momentum thickness which includes body radius term, Eq. (45)
μ	Local mean molecular viscosity
ν	Local mean kinematic viscosity, μ/ρ
ν_{ef}	Local mean effective kinematic viscosity defined by Eq. (14)
ρ	Local mean fluid density
σ, σ^*	Constants used in Eq. (33)
σ_e	Schmidt number for turbulent kinetic energy
σ_x, σ_y	Defined by Eqs. (38)
τ_0	Local total shear stress (molecular + turbulent)
$\vec{\tau}$	Shear stress tensor defined by Eq. (37)
τ_{xy}, τ_{yx}	Defined by Eq. (40)
ϕ	Defined by Eq. (18)
Φ	Defined by Eq. (19)
χ	Defined by Eq. (18)
X	Defined by Eq. (16)

ψ Variable used in Eq. (33)

ω Turbulent dissipation rate

SUBSCRIPTS

aw   Adiabatic wall

c   Airfoil chord length

e   Edge condition

local   Local condition

m   Denotes middle region of boundary layer

o   Total condition; also denotes outer region of boundary layer

w   Wall condition

s   Based on body length

∞ Undisturbed free-stream condition

δ^* Based on boundary-layer displacement thickness

θ Based on boundary-layer momentum thickness

SUPERSCRIPTS

'   Denotes fluctuating quantity

—   Denotes nondimensional quantity, except $\overline{\delta^*}$

SPECIAL NOTATION AND CLARIFICATION

$<\;>$ Denotes time average, e.g., $<uv> = $ limit $t \to \infty$ $1/2t \int_{-t}^{t}(uv)dt'$ The variables denoted in the nomenclature as mean quantities are understood to be time averaged.